MULTIPATH DETECTION AND MITIGATION IN URBAN ENVIRONMENTS

A THESIS

SUBMITTED TO THE DEPARTMENT OF AERONAUTICS AND ASTRONAUTICS

AND THE COMMITTEE ON GRADUATE STUDIES

OF STANFORD UNIVERSITY

IN PARTIAL FULFILLMENT OF THE REQUIREMENTS

FOR THE DEGREE OF

ENGINEER

Shiwen Zhang

May, 2020

This dissertation is online at: http://purl.stanford.edu/mh103bc2038

Approved for the department.

Todd Walter, Adviser

Approved for the Stanford University Committee on Graduate Studies.

Stacey F. Bent, Vice Provost Graduate Education

This signature page was generated electronically upon submission of this thesis in electronic format. An original signed hard copy of the signature page is on file in University Archives.

Abstract

The Global Navigation Satellite System (GNSS) has become more and more widely used in commercial applications such as smart phones, cars, and drones. GNSS is one of the core technologies used for automotive navigation. For consumer automotive applications, it is typically the only navigation system that provides precise absolute positioning and timing. As transportation technology moves towards greater autonomy, the need for and the reliance on precise GNSS with integrity becomes increasingly urgent. For terrestrial applications, multipath becomes the biggest challenge having GNSS with high accuracy and high integrity.

This work explored and examined several approaches to detect and mitigate multipath using newly available resources and technologies. A multipath detection method using three-dimensional (3D) building model with statistical ray tracing was developed that provides better resilience toward initial user position error than deterministic ray tracing and does not rely on redundancy in received GNSS measurements. A multipath mitigation method using multi-frequency signals was also developed that leverages the new civil signals and the correlation in multipath characteristics between different frequency signals from the same satellite to estimate and remove multipath effect on correlation function. Finally, a mapping methodology to infer obstacles in the environment using obscured and unobscured rays was proposed and algorithms were developed to generate 3D maps using GNSS measurements.

Acknowledgments

The work in this thesis would not be possible without the generous help and support I have received from many people.

I would first like to thank my principal advisor Prof. Per Enge for his guidance and support in the early stage of my research and for all the encouragement and inspirations he had offered me. I would also like to thank Prof. David Powell for stepping out as my advisor after Prof. Enge's passing to provide his support and encouragement during a difficult time of my graduate career. I would like to thank Prof. Todd Walter for helping me finish up my research work and for his expertise and advice throughout my graduate research years. And I would like to thank Dr. Sherman Lo for his consistent guidance, mentorship, and all the tangible help he has provided me throughout my entire graduate career. Special thanks are due to Dr. Yu-Hsuan Chen for all his technical support and dedicated time to help me set up equipment and collect data for my research.

I'm also grateful for all my colleagues at Stanford GPS lab: Dr. Eric Phelts, Dr. Juan Blanch, Dr. Sam Pullen, Dr. Tyler Reid, Adrien Perkins, Andrew Neish, Kazuma Gunning, Fabian Rothmaier. I appreciate the advice, help and collaboration they've provided. And I'm grateful for Dana Parga for her administrative support.

I would like to acknowledge the Stanford Center for Positioning, Navigation, and Timing (SCPNT) and the Center for Automotive Research at Stanford (CARS) for their financial support of this work.

I would also like to thank Uber Technologies, Inc. for supporting my internship work that formed a significant portion of this thesis. I'm very grateful for my mentor, Miles Detrixhe, for his guidance and support during my internship and for helping me with the

effort of publishing my internship work. Special thanks are due to Andrew Irish, Praveen Gorthy, and many other colleagues on the Sensing and Perception team for their support and collaboration.

I am especially thankful for all my friends for their love and support and friendship and it is impossible to mention them all in these limited pages: Glen and Paula Davis, Ben and Mariela Schaftel, Dan and Fia Thomas, George and Holly Korir, Art and Carol Heck, Serena Lin, Adrienne Ivey, Jennifer Wu, Kelsie Zhao, Dorothy Kang, and many others who have showed tremendous love to me and brought immense joy in my life.

Finally, I am beyond grateful to my parents, Xiaofang Li and Hanwu Zhang, for their unconditional love and support throughout my life. I am also grateful to my fiancé Andrew Zhao, who never stopped believing in me and has always been selflessly supportive and loving toward me.

Table of Contents

List of Figures

List of Tables

1. Introduction

The Global Navigation Satellite System (GNSS) has become more and more widely used in commercial applications such as smart phones, cars, and drones. GNSS is one of the core technologies used for automotive navigation. For consumer automotive applications, it is typically the only navigation system that provides precise absolute positioning and timing. This is even true for autonomous road vehicles. Railway as well is moving towards use of GNSS for positive and automatic control due to its accuracy, ease of use and ubiquity. As transportation technology moves towards greater autonomy, the need for and the reliance on precise GNSS with integrity becomes increasingly urgent. For terrestrial applications, multipath becomes the biggest challenge to having GNSS with high accuracy and high integrity. This thesis presents and examines several approaches to detecting and mitigating multipath by leveraging the advancement in technology including higher computing power, growing availability of maps, and new addition of civil signals. This chapter discusses some of the fundamental background of GNSS multipath and introduces the most relevant prior art on GNSS multipath research. And the layout of the rest of the thesis is described.

1.1 Background

1.1.1 GNSS Error Sources

GNSS range error can be categorized into several sources and is usually grouped by where they originate. There are several errors emanating from the space segment including ephemeris, satellite clock and signal deformation. The ephemeris errors are those resulting from a difference in satellite position as calculated from the orbital parameters used, usually

from the satellite's broadcast message, and the true satellite position. Satellite clock errors are due to the difference between the implicit satellite time from the satellite broadcast and the true reference time used by the satellite system. The broadcast message can correct from some of the error such as drift rate. Signal deformation errors are caused by deviations of the broadcast signal from the true signal. Propagation errors include those caused by earth atmosphere or obstacles along the signal path. The most common errors caused by Earth's atmosphere are ionospheric delay and tropospheric delay relative to radio propagation travel in a vacuum. Obstacles along the signal path can cause total obstruction of the signal, signal fading, signal scattering, or reflection of the signal. These are local to the user position and may differ significantly even for users that are quite nearby. A GNSS receiver hardware and software can also induce error in the signal's range measurement and such errors are commonly grouped in receiver noise.

Ephemeris and satellite clock errors can usually be corrected by obtaining information from GNSS correction source such as a Satellite Based Augmentation System (SBAS) or a Precise Point Positioning (PPP) service. Another way to compensate for combined ephemeris and clock errors is to use local area differential GNSS corrections. Atmospheric errors can be corrected by using an ionospheric / tropospheric model or differential GNSS (such as SBAS and local area corrections). The receiver noise effect can usually be smoothed out over time through carrier smoothing. Multipath errors, since they are localized to the user, must be corrected by the user equipment. This may be done through antenna technology, receiver processing or both. However, the residual errors can still be very large even with such mitigation.

1.1.2 GNSS Challenges in Urban Environments

Multipath refers to the phenomenon when satellite signals are reflected before reaching the user receiver. Such reflections can cause significant error in user's pseudo range measurements which then result in large errors in the navigation solution.

The multipath environment in aviation is generally benign as the only surfaces that cause multipath are on the body of the aircraft. Standard conservative multipath models for airborne multipath have very low error contributions [1]. This is because there is little strong reflected signal. Even when there is a strong reflected signal, on commercial aircraft, large surfaces that can reflect signals to the GNSS antenna, usually located on the front top of the aircraft, are tens of meters away. The signal path difference between reflection and direct line-of-sight (LOS) is usually large enough that multipath error is easy to detect and correct. Also, the airborne user experience very few strong multipath signals given that there are few surfaces that can produce it. This allows for mitigation by outlier detection and exclusion. For example, if there is only one multipath-corrupted satellite signal, it can be easily detected by an outlier detection algorithm like the Fault Detection and Exclusion (FDE) algorithm in Receiver Autonomous Integrity Monitoring (RAIM).

The growing use of autonomous systems such as self-driving cars and Unmanned Aerial Vehicles (UAV), has made localization and navigation with high accuracy and integrity in urban environments much more essential. Multipath is a significant source of error in the urban environment and can cause huge positioning error in user's navigation solution. Buildings can not only block GNSS signals, causing these signals to be unavailable to users, but they can also induce reflection from multiple directions, even causing double- or triple-

reflection. The reduced availability of signals as well as the complexity of multiple reflections make multipath error much harder to detect and correct.

Integrity is essentially how much trust we can place on the navigation solution for our desired uses – which means being able to provide a high confidence bound on our position errors. Identifying and mitigating multipath is also key to having navigation integrity in the urban environment. If our error models do not consider multipath, the position bounds derived from those models will not be adequately safe. Conversely, if we always use the worst-case multipath model, our bounds could be excessively conservative and large making GNSS difficult to use for precise navigation. Hence identifying multipath and properly modeling its effect is important in providing position solution with integrity that is useful for urban applications. Identifying and reducing the effect of multipath would enable GNSS to be a primary component in many high integrity applications such as railway control and autonomous vehicle operating in urban environments.

1.2 Prior Art

Multipath errors have been an important consideration for GNSS almost since its inception and much research has be conducted on its detection and mitigation. We can classify the approaches taken into several categories: antenna, measurement, signal processing, and map based multipath prediction. This thesis exclusively deals with the effect of multipath on code phase measurements, so the literatures included here are also those directly related to the detection and mitigation of code multipath error.

Antenna based approaches modify a traditional antenna structure to reduce or estimate multipath components. One approach is to the prevent multipath from entering the antenna.

Most antennas have some reduced sensitivity to multipath by having much higher gain for the right-hand circular polarization (RHCP) of GNSS signals. As single reflection multipath has mostly left-hand circular polarization (LHCP), this attenuates the incoming multipath. Multipath limiting antenna (MLA) adapts the antenna design to limit signals coming from very low and negative elevation angles relative to the antenna ground plane as multipath tends to come from such angles in many applications [2]. MLA tend to be bulky and the assumption that multipath is from low elevation relative to the ground plane does not hold in all environments or applications. Another approach is to estimate the multipath component using multi-antenna based spatial techniques. For example, a multi-antenna system using a set of five antennas was proposed to estimate and remove multipath error based on the spatial correlation of received signals [3]. But this type of system is expensive and large in size, which makes it difficult to be implemented in commercial ground vehicles.

Multipath prediction and mitigation based on maps and other measures of the external environment have also been proposed. Reference [4] proposes a multipath detection technique based on using an upward-viewing infrared camera to identify the open sky and hence directions where direct and multipath signals may come from. Satellites that are blocked by buildings, thus resulting in non-line-of-sight (NLOS) signals, were discarded when calculating position solutions. But this technique cannot reliably detect the case when both the line-of-sight (LOS) signal and the reflected signals arrive at the receiver.

Multipath detection methods using 3-dimensional (3D) environmental building model for multipath prediction have also been heavily studied. Given that such maps are rapidly being generated for urban environments, particularly for autonomous driving applications [5], it

makes sense to use such models to aid GNSS integrity. One such method uses a simple building model derived from elevation-enhanced maps to predict NLOS signal propagation [6]. In [7], the authors incorporated the ray-tracing model with GPS/INS data fusion to reduce multipath error. And the authors in [8] simulated both LOS and NLOS signals through ray tracing and took into account the uncertainty of the building model.

Measurement processing include examining the pseudo range and performing redundancy checks such as RAIM. These can detect and exclude excessive multipath or NLOS signals. However, redundancy checks are suitable for situations where there are relatively few faulted (multipath affected or NLOS) signals relative to overall signals. While this is an appropriate assumption for an aircraft in flight, a deep urban canyon may have as many or more multipath and NLOS signals as clean LOS signals.

Multipath mitigation can also be achieved inside the GNSS receiver through various signal processing techniques and receiver architecture designs. Code based techniques focus on the effect on the autocorrelation function of the GNSS signal and attempt to either detect or mitigate the effect of multipath. Narrowly spaced early and late correlators can be used to reduce tracking error in the presence of multipath by reducing the effect of distortion on the correlation function [9]. The Multipath Estimating Delay Lock Loop (MEDLL) [10] uses multiple complex correlators to estimate the delays, amplitudes and phases of direct line of sight (LOS) and reflected multipath signals using maximum likelihood estimation theory and removes the estimated effect of multipath on distorted correlation function using the modelled multipath parameters. The Early-Late-Slope (ELS) technique [11] used two pairs of narrowly spaced early and late correlators to estimate the slope on each side of the correlation peak and achieves higher reduction of multipath error in differential GPS

position solution than the standard narrow correlator technique. The early-late-phase (ELP) technique described in [12] is a method to detect multipath based on the carrier phase difference between the early and late correlators and can be applied to both single- and dual-frequency receivers.

While multipath is often thought of as a nuisance to the radio navigator, it can also provide utility, especially if we are able to accurate predict it. For example, shadow matching [13] uses 3D building model to predict satellite visibility and compares the predicted satellite visibility with the measured visibility to determine position. Furthermore, having direct and multipath signals can help generate 3-D building maps with the quality of the modeling partly dependent on our ability to detect multipath and LOS signals. In [14], a 2.5D mapping algorithm using GNSS signals was proposed that computes building footprint by creating a 2D density map that keeps a list of elements with the altitude and LOS / NLOS classification result at each 2D coordinate. It then estimates building heights by calculating the likelihood matrix from the density map to predict the most probable structure height at each 2D coordinate. A similar approach was proposed in [15] where low-SNR GNSS rays were projected onto the 2D ground plane to generate a 2D density map, and a clustering algorithm was used to identify building footprints; finally, 3D buildings were constructed using the building footprints and the low-SNR rays. A Bayesian approach using Loopy Belief Propagation algorithm for mapping was developed in [16] that uses GNSS SNR to predict the likelihood of a GNSS signal being blocked, and a factor graph to represent the posterior distribution of the 3D environment.

1.3 Organization of Thesis

In this thesis, two approaches for detecting and mitigating GNSS multipath and NLOS pseudoranges are presented. This thesis also develops a methodology of generating 3D building maps using direct and multipath GNSS signals.

Chapter 2 of this thesis provides the relevant background on GNSS multipath.

Chapter 3 describes the developed approach to detect multipath using 3D building model. A statistical model was developed to improve prediction error caused by user position error and building model error in the deterministic approach. Simulation results and experimental results are presented. Results are also compared against the RAIM FDE algorithm to evaluate the performance of the algorithm.

Chapter 4 describes the approach to detect and mitigate multipath using multi-frequency signals. This approach leveraged the new civil signals and the correlation of multipath characteristics across different frequencies to mitigate multipath. Two mathematical formulations are discussed, and simulations are performed to validate the multipath model and to compare the performance between the two formulations.

Chapter 5 describes three probability-based voting algorithms to generate 3D building maps using GNSS signals and provides a methodology to infer obstacles in the surroundings using GNSS rays. Both simulation and experimental results are presented and performance of the three algorithms are evaluated and compared.

Chapter 6 summarizes the key findings and the conclusions of the methods and algorithms presented in this thesis and provides ideas for future work.

2. The Multipath Problem

Multipath in GNSS is the term used to describe the phenomena of having indirect signals, i.e. signals that have reflected off of another surface before encountering our receiver antenna, in our measurements. Multipath, particularly mitigating its deleterious effects on ranging and positioning, has been a major topic of research since the birth of GPS. This chapter provides the necessary background on multipath characteristics that forms the basis for the detection and mitigation approaches that will be introduced in the later chapters of this thesis. Section 2.1 provides an overview of multipath and how it can affect range error. Section 2.2 describes a simple physical model of reflection suitable for modeling multipath using deterministic ray tracing. Section 2.3 then presents the effect of multipath on GNSS auto correlation function (ACF). Modeling the effect on ACF provides another mechanism for determining the presence and characteristics of multipath.

2.1 Overview of Multipath

GNSS multipath comes in two major forms with each form creating different challenges in detection and mitigation efforts and has a different effect on GNSS range error. The two types of multipath are demonstrated in Fig. 1. The first type of multipath, shown in Fig 1a, occurs when the direct line-of-sight (LOS) signal from the satellite is blocked by obstacles and only the reflected signal is received at the receiver. The receiver mistakes the reflected signal as the LOS signal, and causes error in range measurement. This scenario is also commonly referred to as non-line-of-sight (NLOS). The second type of multipath, shown in Fig 1b, occurs when both LOS and reflected signals are received and the reflected signal interferes with the LOS signal. The reflected signals interfere with the direct signal, causing

distortion in the correlation function as well as signal strength variation. While both forms create errors in range measurement, the former can create unlimited range errors while the latter may only create more limited range errors and generally more rapid fluctuations in received signal strength.

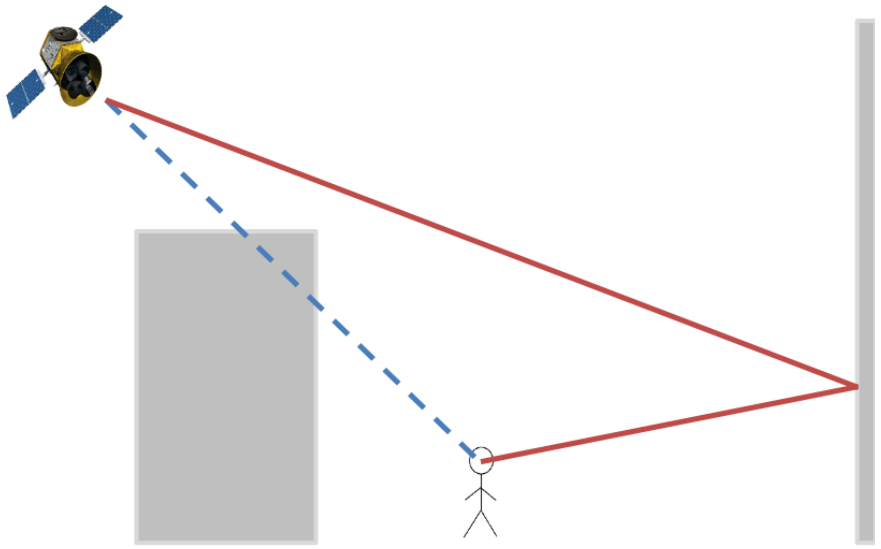

(a)

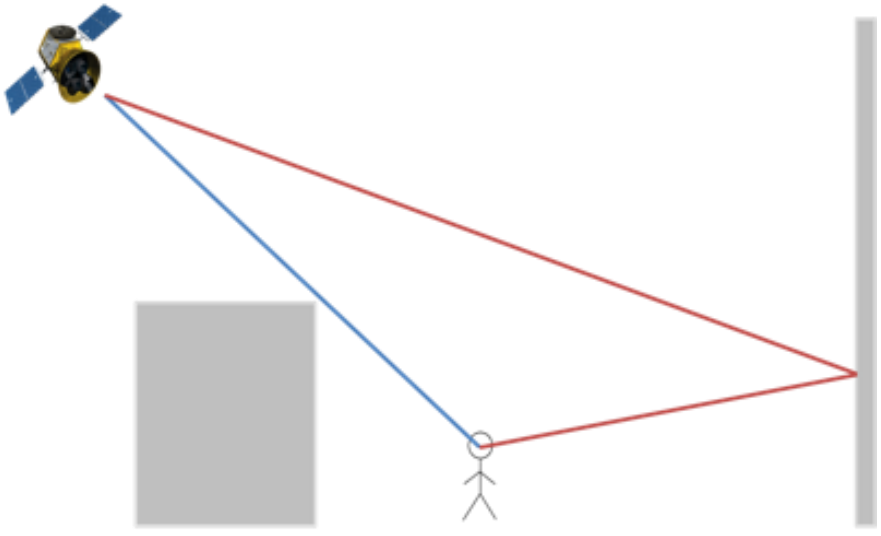

(b)

Fig. 1. (a) Multipath scenario where LOS signal is blocked and reflected signal is received - NLOS; (b) multipath scenario where both LOS and reflected signal are received.

We can show the effect of multipath on GNSS range error through simulation using the scenario shown in Fig. 2. A typical urban street with buildings on both sides of the street is shown in Fig. 2a. Fig. 2b shows the multipath range error versus the distance between the car and the building on the left. Depending on the relative location of GNSS receiver to the side of the street, the signal from a low elevation satellite can generate the two different types of multipath. If the car (receiver) is on the left as shown in Fig. 2a, its line of sight to the satellite is blocked by the building on the left and hence it cannot receive a direct LOS signal from the satellite. Instead, it only receives the reflected signal from the building on the right. Since this is the only signal, the receiver mistakes this reflected signal as the LOS signal and measures a range that is longer than reality, which therefore causes a positive range error. The multipath range error is given by the range difference between the LOS signal and the NLOS signal. If the car/receiver is on the right side on the street (closer to the building on the right), it will receive both the LOS and the reflected signals. The receiver will then process a signal that is a combination of these two signals. They will cause the receiver to measure a range that is derived from the LOS and NLOS signals resulting in errors in this range measurement. The magnitude of the range error depends on many factors such as the wavelength of the signal, and the true difference between LOS and reflected signal.

2.2 Signal Propagation Model

GNSS multipath is the reflection of satellite signals and it follows the law of reflection for electromagnetic waves. The law of reflection states that the incident ray, the reflected ray, and the normal to the reflector surface all lie in the same plane. The angle of reflection is the angle between the surface normal and the reflection ray. The angle of incidence is the angle between the surface normal and the incident ray. Furthermore, the law has the angle

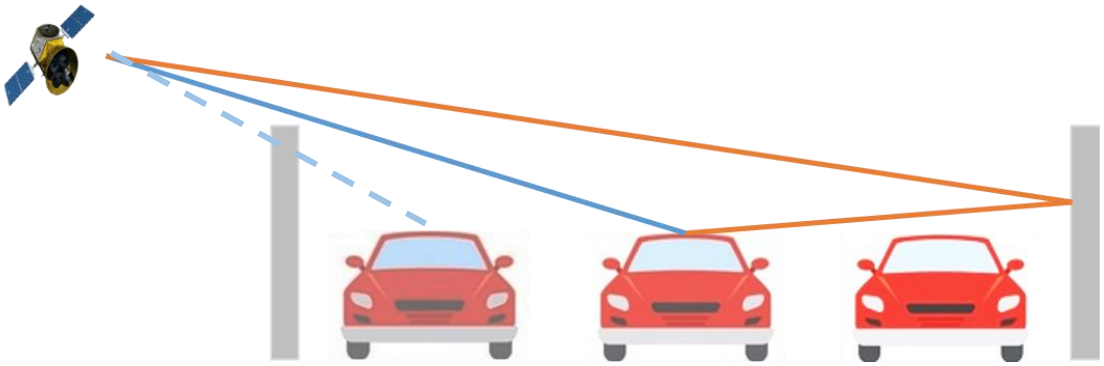

(a)

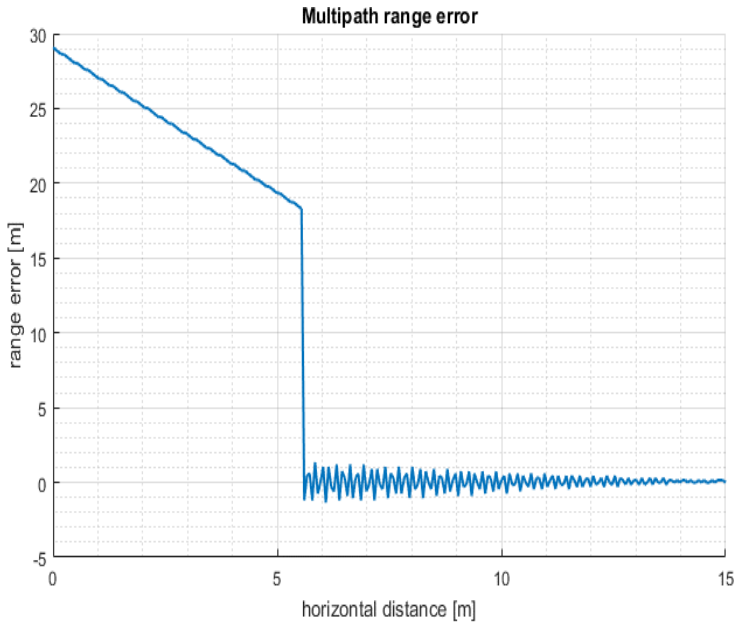

(b)

Fig. 2. (a) Urban scenario with buildings on both sides of the street and a low elevation satellite to the left; (b) multipath range error plotted against the distance to the left building.

of reflection being equal to the angle of incidence as shown in Fig 3. The law of reflection forms the basis of deterministic ray tracing. If we know the location and orientation of the reflector, we can trace the reflected GNSS ray from the satellite to the point of incidence and then to the receiver. The path that the reflected signal travelled provides us valuable information on how the range measurement is impacted by multipath. This is a reasonable but simplistic model for multipath that only takes into consideration specular reflection. More complex scattering and fading effect in signal propagation can also impact LOS and reflected signal paths and signal strength. For example, total blockage of signal does not occur as soon as the signal touches the boundary of the obstacle. But rather, the signal bends around the corner of the obstacle and causes decrease in signal strength rather than

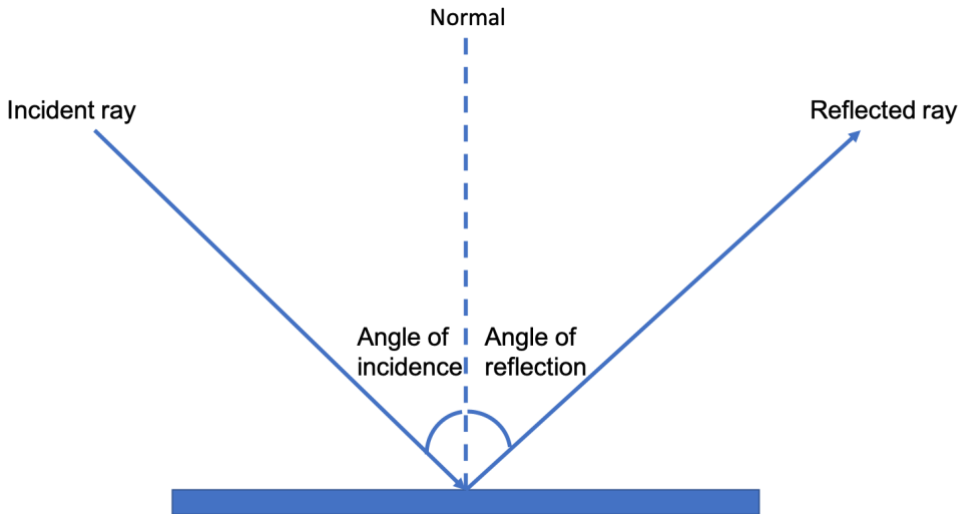

Fig. 3. Law of reflection.

total loss of signal. But since GNSS signals are transmitting at such low power, the effect of diffraction is negligible, and a simple reflection model based on specular reflection is usually sufficient. For example, [6] and [8] both used ray tracing and building model to predict the presence of reflection signals according to specular reflection alone. However, the limitation of using deterministic ray tracing to predict multipath is that we need to know

the location of the user to predict the presence of multipath, but the location of the user is the very unknown that we are trying to estimate accurately under multipath. Chapter 3 deals with the detail of using ray tracing and building model to predict multipath and discusses how the limitation of deterministic ray tracing is handled.

2.3 Correlation Function

GNSS signals transmit Pseudo-Random Noise (PRN) codes modulated into a carrier signal and use correlation operation to measure the range of the incoming signal. PRN codes take on values of +1 or –1. The codes are designed with special correlation properties such that the correlation between different PRN codes is very low and the correlation between different code offsets of the same code is also low. For example, GPS C/A code repeats every 1023 bits (known as chips) and modulates at 1.023 megahertz (MHz) chipping rate. The auto-correlation function (ACF) for a GNSS signal is defined in the time domain as

$$R(\tau) = \frac{1}{T_{code}} \int_0^{T_{code}} x(t)x(t-\tau)dt$$

where $x(t)$ is the PRN code and T_{code} is the period of $x(t)$. When $\tau = nT_{code}$ where $n = 0, \pm 1, \pm 2, \cdots$, the ACF takes on the maximum value of 1.

$$R(\tau) = \frac{1}{T_{code}} \int_0^{T_{code}} x^2(t)dt = \frac{1}{T_{code}} \int_0^{T_{code}} 1\ dt = 1$$

The ACF can be approximated as a triangular function with its peak at $\tau = 0$, and with the base of the triangle equals to $2T_C$, where T_C is the duration of a single chip.

Each GNSS satellite transmits its signal with a unique PRN code sequence known by the GNSS receiver. And the receiver generates a replica of the code sequence and tries to match it with the received code using ACF. Once a match is found, the time of

transmission of the signal can be determined and the receiver can measure range, or more accurately pseudo range, using the difference between the time of transmission and time of arrival as measured by the receiver.

In a standard GNSS receiver, two or three replicas are generated, and the goal is to have at least one replica falling on each side of the correlation triangle. The one on the rising side of the triangle is called the early correlator and the one on the falling side is called the late correlator, as shown in Fig. 4. The offset between the early correlator and the late correlator are fixed and the offset is called correlator spacing. A control loop is used to match the output of auto correlation function for early and late correlators. When the early correlator output matches the late correlator output, the midpoint of the early/late correlators is ideally where the correlation peak resides. The midpoint is where the receiver will assume the correlation is aligned.

Mathematically, if the auto-correlation function is denoted as $R(\tau)$, the early (S_E) and late (S_L) correlator output can be expressed as:

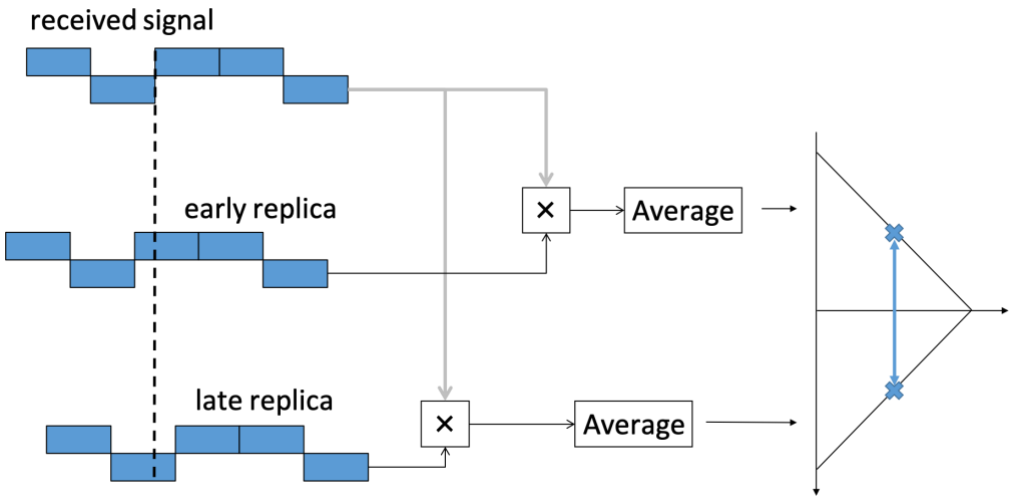

Fig. 4. Early and late correlators in a GNSS receiver.

$$S_E = R(\tau_e - \frac{\delta}{2})$$

$$S_L = R(\tau_e + \frac{\delta}{2})$$

where τ_e is the error of the code delay estimated at the receiver and δ is the early and late correlator spacing. And τ_e is estimated by having the control loop attempt to equalize the two correlator outputs as follows:

$$S_E - S_L = 0$$

This is also the formula used to generate Fig. 2b.

As shown in Fig. 5, when LOS signal and a reflected signal are both received, the mixture of both signals results in distortion in the shape of the correlation function. The blue triangle is the ACF of the LOS signal only and the left-most black dashed line represents the calculated peak of the LOS only ACF. The correlation function with the reflected signal is shown in red and is shown as being weaker as it is usually attenuated by the reflection. The overall correlation function is represented by the yellow dotted line. The assume alignment, i.e. the midpoint between the equalized early and late

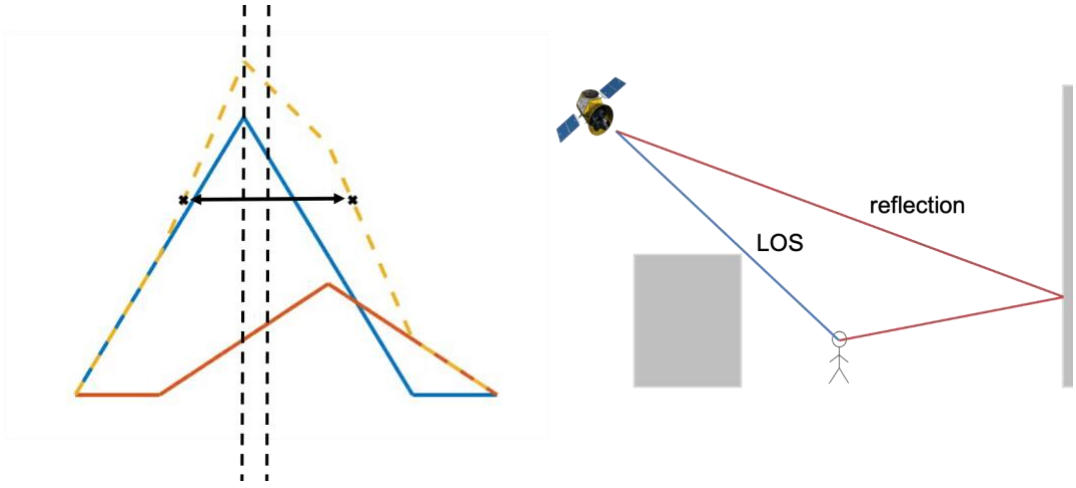

Fig. 5. Auto corelation furnction distortion in the presence of reflection.

correlator, of the correlation function from the combination of the LOS and NLOS signals, is given by the black vertical dashed line on the right. Note that this is not the peak but a receiver with 2 or 3 correlators cannot easily know this. The final range error caused by this distortion is the gap between the two black vertical dashed lines. And this error is the multipath range error.

Now consider the same multipath scenario but narrowing the spacing between early and late correlators, it can be seen by comparing Fig. 5 and Fig. 6 that by simply narrowing the spacing between correlators, the measured multipath range error is significantly reduced [9]. And since the distortion of ACF is a strong indication of the presence of multipath, more correlators can be implemented in the receiver to better estimate the shape of the ACF to estimate and mitigate multipath. This is the idea behind Multipath

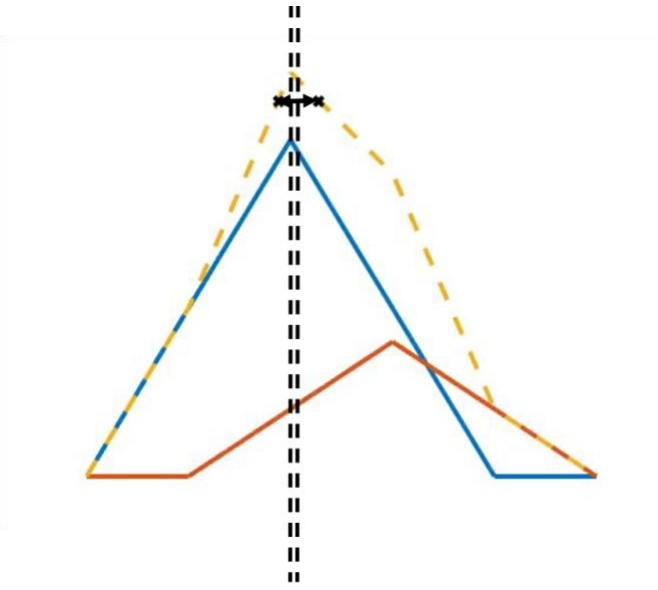

Fig. 6. Multipath error with narrow correlators.

Estimating Delay Lock Loop (MEDLL) [10]. Chapter 4 will discuss how to use multiple correlators to estimate multipath parameters and apply the MEDLL technique to multiple frequency signals to better aid the mitigation effort.

3. Three-Dimensional Building Model

This chapter describes, develops and examines a multipath detection and exclusion method leveraging ray tracing on a three-dimensional (3D) building model to predict the signal paths at the estimated user position. The overall goal of the work is to allow us a way of providing integrity in situations that may overwhelm the detection capabilities of RAIM. For practicality, we have to handle imperfect building models and so sensitivity analysis on the building model is utilized to manage these errors. This not only helps understand how imprecision in our building model may affect detection but also provides a potentially useful mechanism to estimate the confidence level of the prediction. Satellite exclusion is then performed based on the parameters derived from our ray-tracing model to test the overall performance and sensitivity.

3.1 Ray Tracing Model

Ray tracing can be used to predict the presence of both LOS and reflected signals given a satellite-user geometry. A 3D building model was developed for ray-tracing simulation and multipath prediction. The site chosen for simulation and testing is the Engineering Quadrangle (Quad) at Stanford University (Fig. 7). This site contains four buildings with each building being three-story high. The building model was constructed using building corner coordinates and building heights estimated from Google Earth. Detailed structure of the building walls and roofs were not captured in the model to simplify the simulation. Trees and other foliage were also not modeled for the same reason. The final building model contains the surface normal vector and the boundaries of each sidewall for all the buildings in the model.

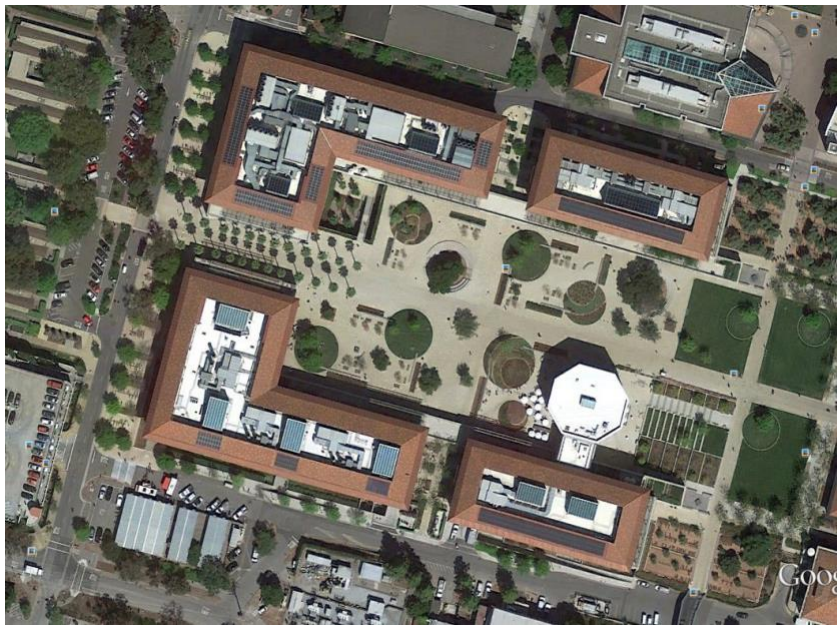

(a)

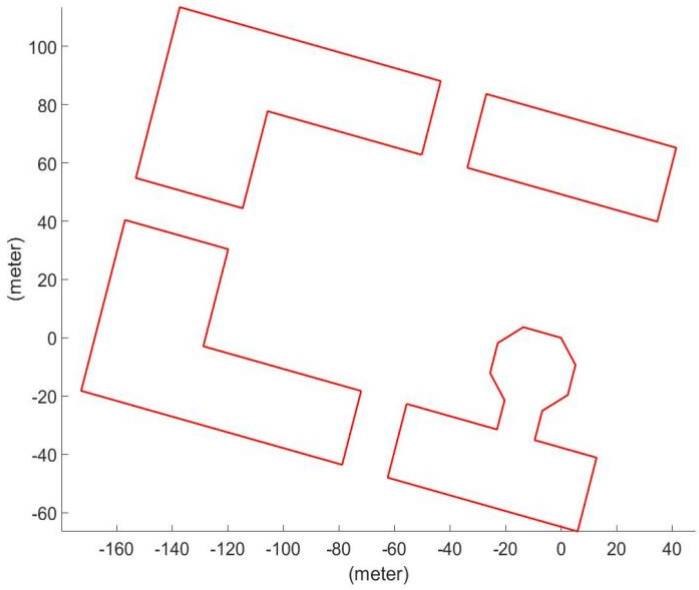

(b)

Fig. 7. (a) Top view of the simulation and testing site at Stanford University; (b) Building model created from Google Earth for simulation.

The ray-tracing algorithm simulates the LOS signal path as well as all the building-reflected signal paths from the satellite to the user receiver. The LOS propagation is simulated by a

straight-line segment connecting the satellite and the user receiver. Then the algorithm checks whether the propagation line passes through any sidewall within its boundaries. Single reflections are simulated using a vector-based ray-tracing method described in [17]. First of all, the satellite-user geometry is used to eliminate reflection surfaces. Sidewalls that are facing the wrong direction relative to the examined satellite are discarded before further simulation for reflection path. And for each of the potential reflection surfaces, a reflection image of the user receiver with respect to the surface is generated. A propagation from the satellite to the receiver's image is then simulated (Fig. 8). If this propagation path intersects with the reflection surface corresponding to the receiver image within its boundaries, the actual reflection path from the satellite to the receiver will be simulated. And if this reflection path is not blocked by any other sidewall, the reflection path will be stored for further calculation. The algorithm continues to find valid reflection paths from all possible reflection surfaces given the satellite-user geometry.

Ground reflection was not simulated since it is assumed that the GNSS antennas can effectively reject signals arriving at low or negative elevation angles. Simulations also showed that double reflection was likely not present in the specific environment. Analysis and simulations on diffraction were also conducted and the results showed that multipath range error caused by diffraction is minimal and can be neglected [18]. Therefore, diffraction and double reflection are both ignored in simulations used to generate model prediction on the experimental data.

3.2 Simulation

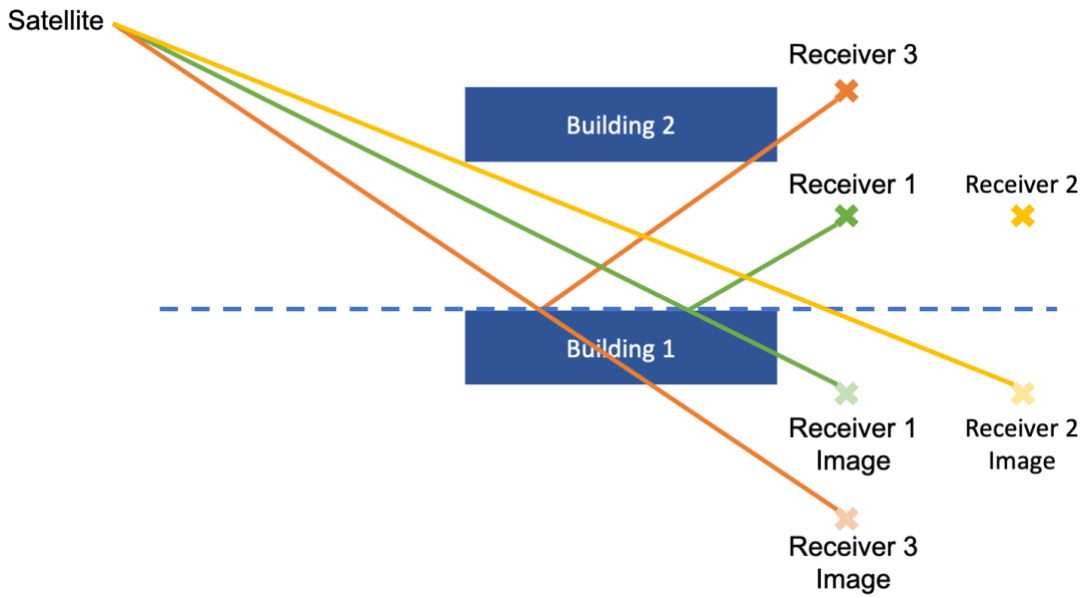

Fig. 8. Simulation of single reflection paths.

Fig. 9 shows the simulation result for users on the ground for a satellite at 90-degree azimuth and 15-degree elevation. Fig. 9a shows the prediction of LOS coverage and Fig. 9b shows the regions where the received signal will be corrupted by signal reflections. The strip pattern in Fig. 9c is the result of interference between LOS signal and reflected signals. And the region with multiple-color strips in Fig. 9c is the region with large range error, which is caused when LOS signal is blocked and only reflected signals are received.

3.3 Sensitivity Analysis

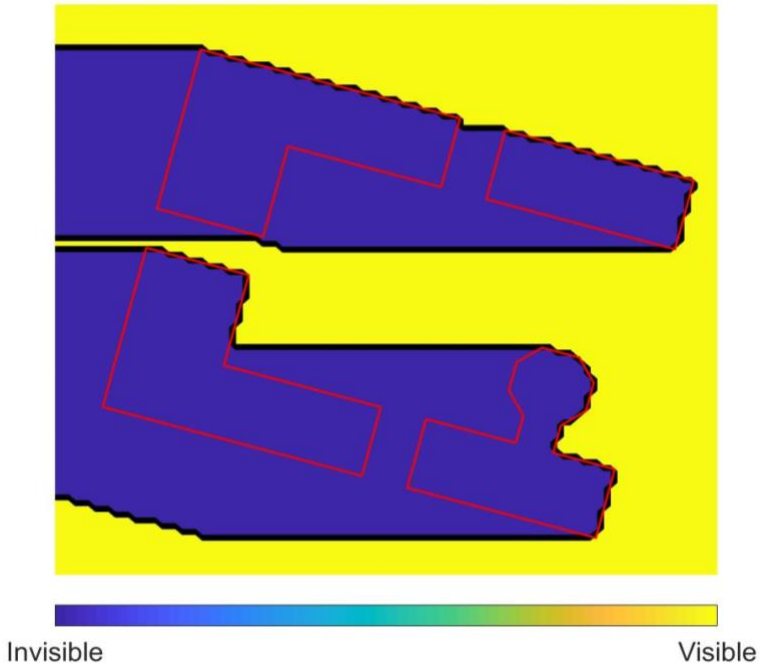

(a)

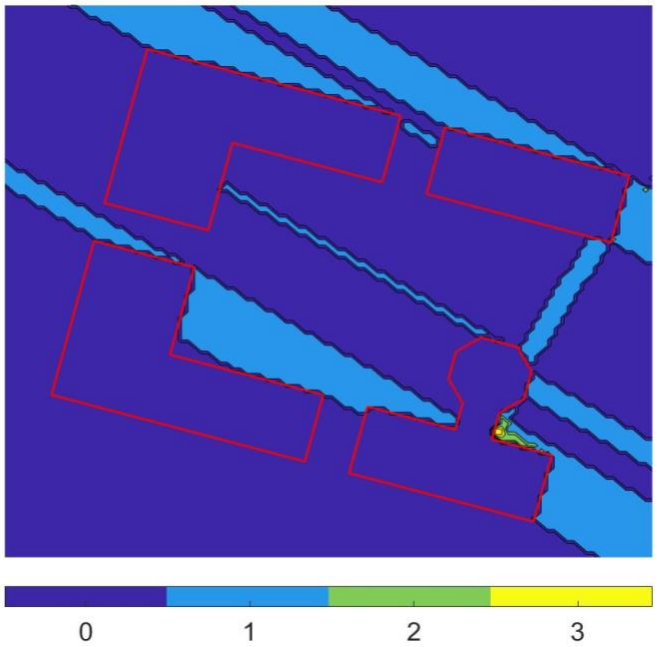

(b)

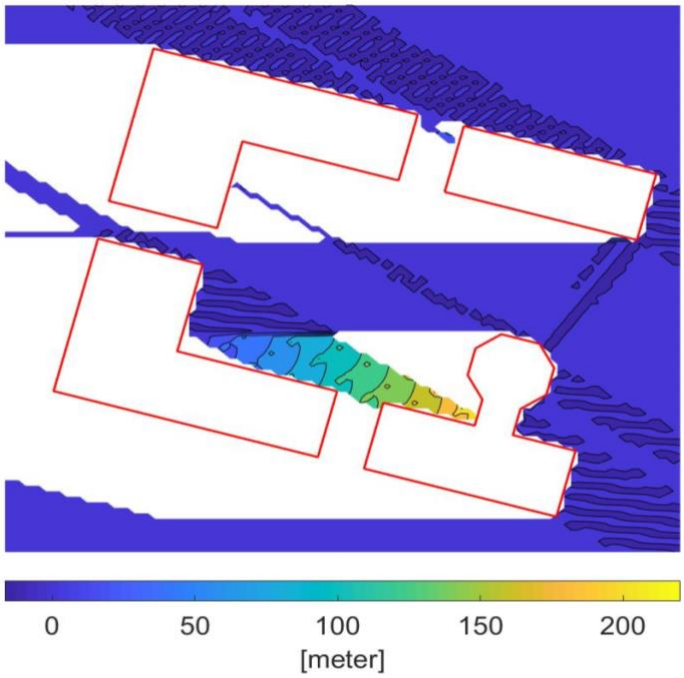

(c)

Fig. 9. (a) Line-of-signt coverage; (b) number of single reflections; (c) multipath range error. Modeled satellite signal is from 90 degree azimuth (North being zero degree) and 15 degree elevation.

While ray-tracing algorithm is a deterministic algorithm, the prediction results are predicated on a precise knowledge of the building surfaces and the user location. Indeed, these two factors are related in ray tracing methods as we care about the relative relationship between the user location and building walls. To improve the robustness of the algorithm given building model uncertainty, a statistical sensitivity analysis with the ray-tracing algorithm was performed whereby building corner and height locations are taken as variable.

Independent and identically distributed uniform noise based on our building model uncertainty was added to each of the building corner locations and heights. Monte Carlo simulation was then carried out on the model with noise for statistical analysis. By

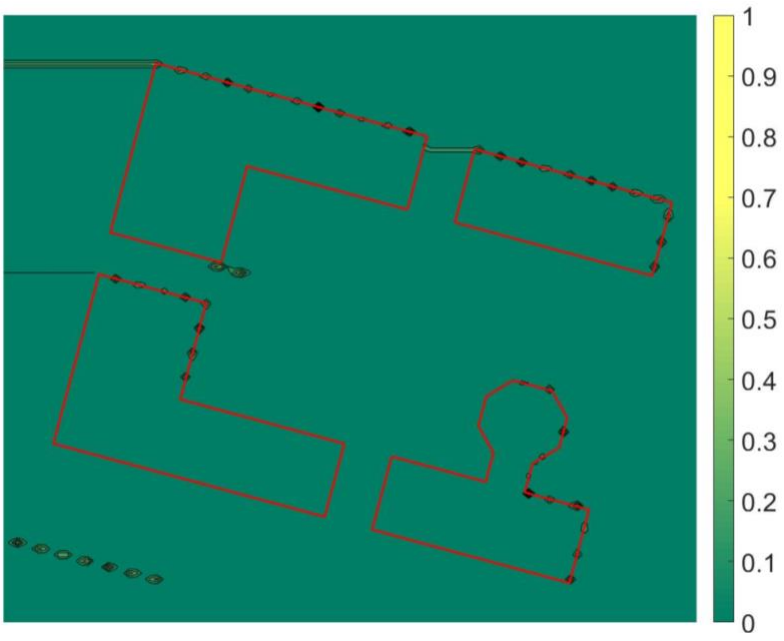

Fig. 10. Probability of disagreement for LOS prediction between the original model and the model with uncertainty for a satellite at 90-degree azimuth and 15-degree elevation.

comparing the difference in prediction between the original model and the model with noise, sensitivity to modeling uncertainty at a particular user location for a particular user-satellite geometry can be estimated.

Therefore, sensitivity analysis helps quantify the confidence level of the model's multipath prediction under modeling uncertainty. Fig. 10 and Fig. 11 are the plots for probability of disagreement for LOS prediction and reflection prediction, respectively, for a satellite at 90-degree azimuth and 15-degree elevation. Let $m_0 = \{c_{0,j}\}$ be the original model where $c_{0,j}$'s are the building corner coordinates. Then $m_i = \{c_{i,j}\}$ is the i^{th} simulation of the model with uncertainty, where $c_{i,j} = c_{0,j} + n_j$ and n_j's are uniformly distributed random variables on the interval $[-1,1]$. Let p_s and p_r be the position of the satellite and the position of the user,

respectively, then the probability of disagreement for LOS prediction for a satellite at p_s and a user at p_r is estimated as follow:

$$\mathrm{P}(m_i(p_s,p_r) = \text{Reflection} \mid m_0(p_s,p_r) = \text{LOS}) = \frac{\sum_i \mathbf{1}(m_i(p_s,p_r) = \text{Reflection})}{n}$$

$$\mathrm{P}(Model\ with\ uncertainty = \text{Reflection} \mid m_0(p_s,p_r) = \text{LOS})$$

$$\cong \frac{\sum_i \mathbf{1}(m_i(p_s,p_r) = \text{Reflection})}{n}$$

where n is the total number of simulations. And similarly, the probability of disagreement for reflection prediction is estimated as

$$\mathrm{P}(m_i(p_s,p_r) = \text{LOS} \mid m_0(p_s,p_r) = \text{Reflection}) = \frac{\sum_i \mathbf{1}(m_i(p_s,p_r) = \text{LOS})}{n}$$

Simulation result shows that for a low elevation satellite, reflection prediction is more sensitive to modeling uncertainty than LOS prediction.

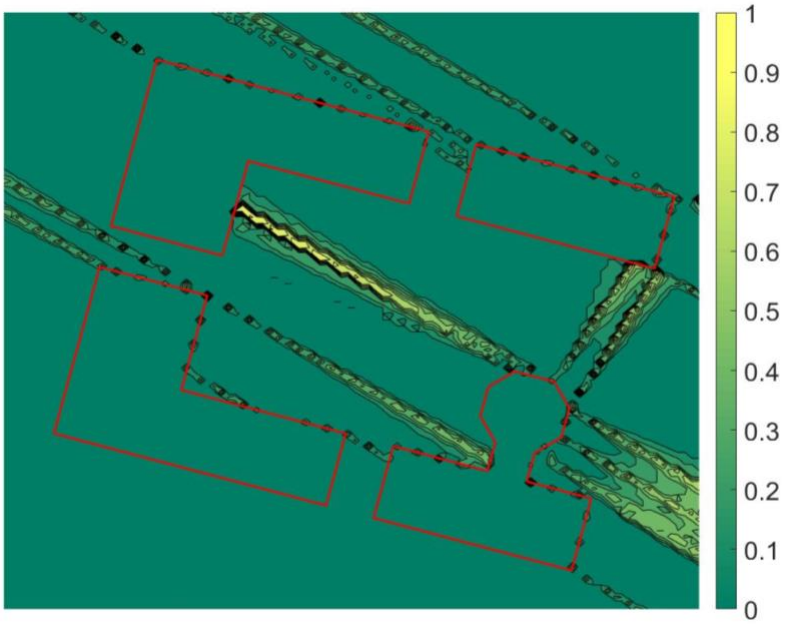

Fig. 11. Probability of disagreement for reflection prediction between the original model and the model with uncertainty for a satellite at 90-degree azimuth and 15-degree elevation.

3.4 Experimental Results

A field test was performed on the Engineering Quad at Stanford University. L1 C/A GPS data were collected at 13 ground locations on the Engineering Quad using a NovAtel ProPak-V3 GNSS receiver (Fig. 12). Carrier smoothing interval was set to 2 seconds, which is the lowest value allowed by the receiver. But since carrier smoothing cannot be turned off completely, some multipath effect, particularly rapidly varying ones, will be smoothed out to some extent. The data collection time was chosen so that both NLOS and multipath receptions were predicted, based on the building model and satellite geometry, to be present at the test locations. In order to maintain a similar satellite geometry during the entire time of data collection, only 10 seconds of data were collected at each location. And the entire data collection process was completed in 12 minutes. Thirty minutes of extended data collection was also conducted, and data were processed using the precise point positioning (PPP) service provided by Natural Resources Canada (NRCan) to obtain the ground truth of the testing points. A sky plot of all the satellites in view at the time of the field test is shown in Fig. 13. There was a total of 10 GPS satellites in view.

3.4.1 GPS Data Processing

GPS L1 pseudorange data were post-processed to remove the common errors including ionospheric error, tropospheric error and satellite clock bias. Ionospheric error corrections were obtained from the Wide Area Augmentation System (WAAS). Tropospheric errors were estimated using the WAAS tropospheric delay model [19].

3.4.2 Detection Algorithms

A total of four algorithms for satellite exclusion were implemented on the collected GPS L1 pseudorange data compared to an all-in-view (unmitigated) solution. Single point positioning solution was calculated at each testing location. The same positioning algorithm using unweighted least squares was applied to all detection algorithms [20].

1) The no exclusion algorithm: This algorithm uses all the received signals to calculate position solutions. This is the all-in-view solution.

2) The residual checking algorithm: The traditional Receiver Autonomous Integrity Monitoring (RAIM) Fault Detection and Exclusion (FDE) algorithm based on consistency checking of pseudorange residuals is used [21]. This algorithm sequentially excludes signals that are inconsistent with the rest until the remaining residuals are consistent with each other according within a specific threshold. The algorithm then uses the remaining

Fig. 12. Field testing locations on the engineering quad.

signals for position solutions. The detection threshold for RAIM-FDE corresponds to a false alarm rate of 0.1 assuming the multipath-free measurement errors follow a zero-mean Gaussian distribution. A detailed description and derivation of RAIM algorithm can be found in [21].

3) The hard exclusion algorithm: This algorithm excludes signals based on the building model's predictions of LOS and reflection. Satellite positions and an initial estimate of the user position were input into the model to generate a multipath prediction for each satellite in view. The initial user position is estimated from the all in view solution and the user height is estimated from the building model. Only the horizontal position from the all-in-view solution was used because the relative height above ground for the user antenna can be easily measured for ground vehicles and we assume that the elevation of the local ground

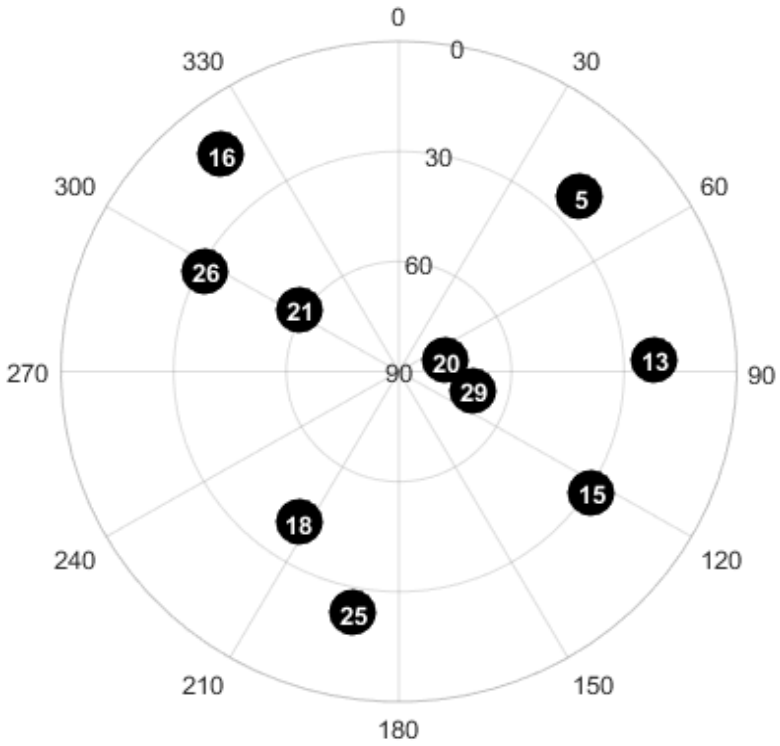

Fig. 13. Sky plot of all the satellites in view at the time of the field test.

level is known. The model outputs two parameters. The first parameter predicts the presence of the LOS signal. The second parameter predicts the presence of the reflection signals. The decision process of the hard exclusion algorithm is shown in Table I. Only satellite signals considered usable are those where we only predict LOS signals are present. All other cases are excluded as the measurement is considered containminated by multipath. This is an extreme approach aimed at maximizing integrity rather than availability. While the model can provide the multipath delay which provides an estimate of the its severity, this more granular information is not used in our current work but may be worth exploring in the future. Detection results from the hard exclusion algorithm showed that accurate detection of multipath signals based on the building model can be affected by two factors: the uncertainty in the model and the accuracy of the initial user position estimate. Therefore, two more detection algorithms were implemented to demonstrate the effect of each of these two factors on the model's detection accuracy.

4) The soft exclusion algorithm: The soft exclusion algorithm performs satellite exclusion based statistical results generated using uncertainty in the building model. Sensitivity analysis was performed at each testing location. Uniform noise with distribution U(-1 m, 1 m) was added to each of the building corner coordinates and building heights. 100 Monte Carlo simulations were carried out on the model. Two sensitivity parameters, one indicating the estimated probability of having LOS signal and the other indicating the estimated probability of having reflection, were generated by averaging over the simulation results. For example, if 30 out of the 100 simulations predict "yes' for LOS, the sensitivity parameter for LOS prediction is 0.3. The decision process of the soft exclusion algorithm is listed in Table II. The table incorporates a basic notion of severity of the multipath in its

decision threshold. The threshold for having a reflection result in excluding the satellite signal is higher if a LOS is believed to be present (prediction is "yes"). This is because multipath error is bounded when LOS signal is present, and error caused by worse satellite geometry may exceed the error caused by multipath in this case. This higher threshold is a representation of the tradeoff between multipath error and satellite geometry.

5) *Hard exclusion initialized with RAIM (Hard + RAIM):* This algorithm is the same hard exclusion algorithm as described before. But instead of using the no exclusion algorithm to obtain an estimate of user position, the position estimate from the RAIM algorithm was used. So this algorithm allows us to examine the sensitivity of hard exclusion's detection performance to errors in initial position. The position solution using RAIM is better in this multipath environment than that from the all-in-view.

TABLE I. EXCLUSION DECISION FOR THE HARD EXCLUSION ALGORITHM

LOS	**Reflection**	**Decision**
Yes	No	Include
Yes	Yes	Exclude
No	Yes	Exclude
No	No	Exclude

TABLE II. EXCLUSION DECISION FOR THE SOFT EXCLUSION ALGORITHM

Sensitivity analysis				**Decision**
Probability of LOS		***Probability of reflection***		
> 0.6	Yes	< 0.8	No	Include
> 0.6	Yes	> 0.8	Yes	Exclude
< 0.6	No	< 0.6	No	Exclude
< 0.6	No	> 0.6	Yes	Exclude

3.4.3 Results and Discussion

Performance of the five detection algorithms were evaluated. Fig. 14 shows the root mean squared (rms) 3D position error at each testing location for the five algorithms plotted against the distances to the first testing location. Position error from the no exclusion algorithm suggests that multipath was present at multiple testing locations with an extreme case at location 7. The hard exclusion algorithm removed several signals and reduced the large position errors that we believe to be due primarily to multipath signals. The performance of the hard exclusion algorithm at locations 3 and 13 was worse than the no exclusion algorithm. This is due to excluding so many signals that satellite geometry was significantly affected. The horizontal dilution of precision (HDOP) was calculated and

plotted in Fig. 15. HDOP at locations 3 and 13 shows that the hard exclusion algorithm

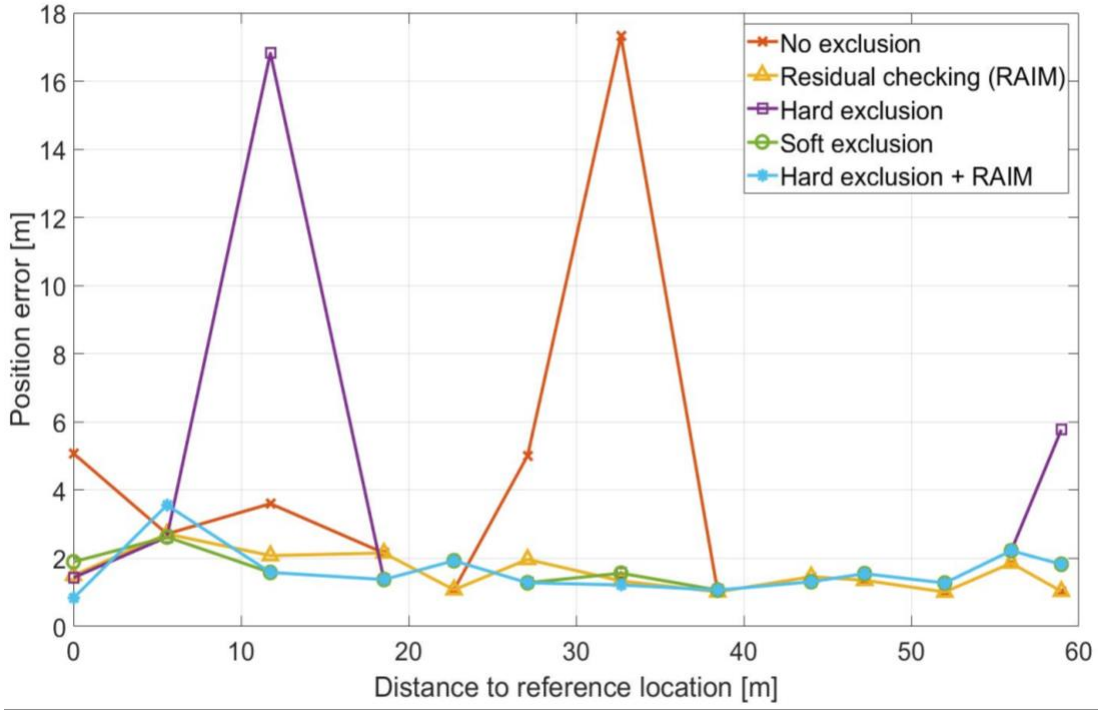

Fig. 14. Position error at each testing location for the five detection algorithms.

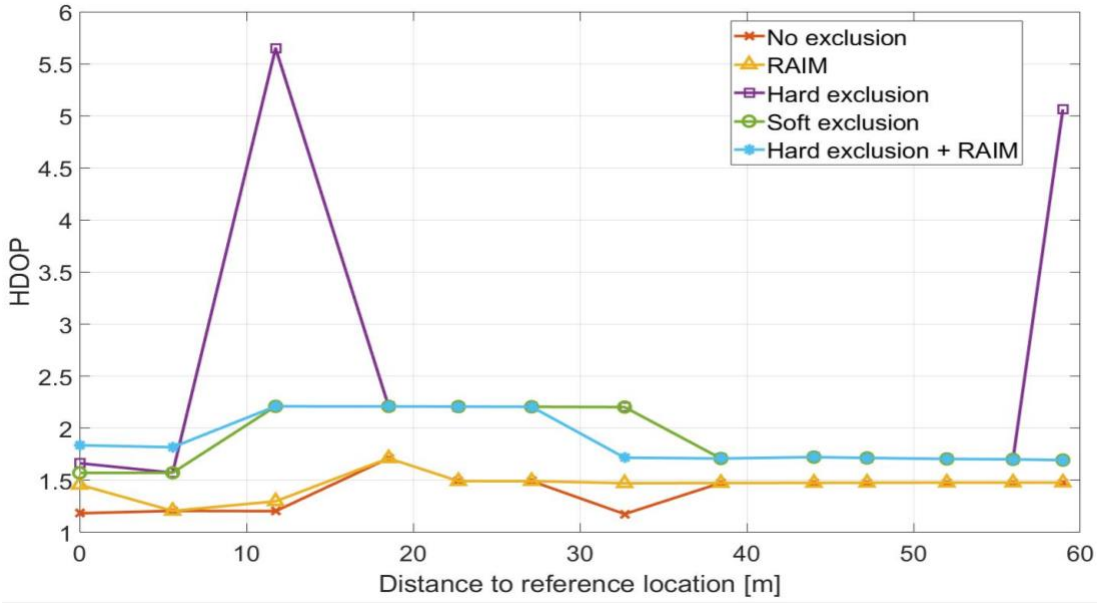

Fig. 15. Horizontal dilution of precision based on satellites used for position solution at each testing location for the five detection algorithms.

removed good signals that did not contain multipath at these locations. The result of the excessive exclusion was poor satellite geometry.

Examination of the hard + RAIM results show much lower errors for locations 3 and 13 which suggests that the initial position error can have a significant effect. The no exclusion and RAIM algorithm both have similar levels of errors for those two locations. But they have different enough positions, as shown in Fig. 16, to result in different decisions by the hard exclusion algorithm. Overall the hard + RAIM algorithm has error below 4 meters for all testing locations, which matches typical GPS performance. Fig. 17 shows hard exclusion results using the true location for initial position. The errors for this algorithm are the same as the errors for the hard + RAIM algorithm, which indicates that the RAIM solution is close enough to the true location of the user for the hard exclusion algorithm to make decisions consistent with the hard + RAIM algorithm.

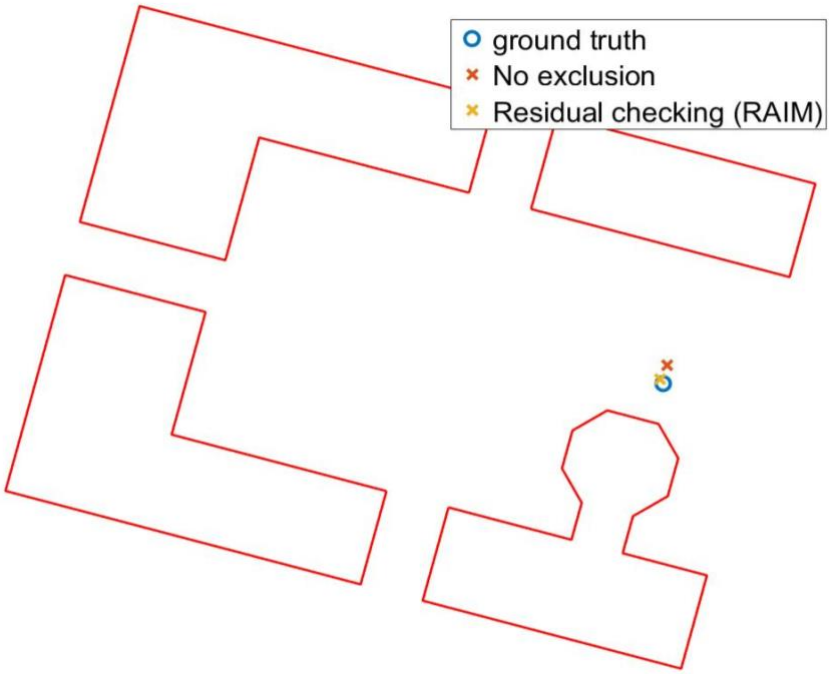

Fig. 16. 2D position plot of ground truth, no exclusion solution, and RAIM solution for testing lcoation 3.

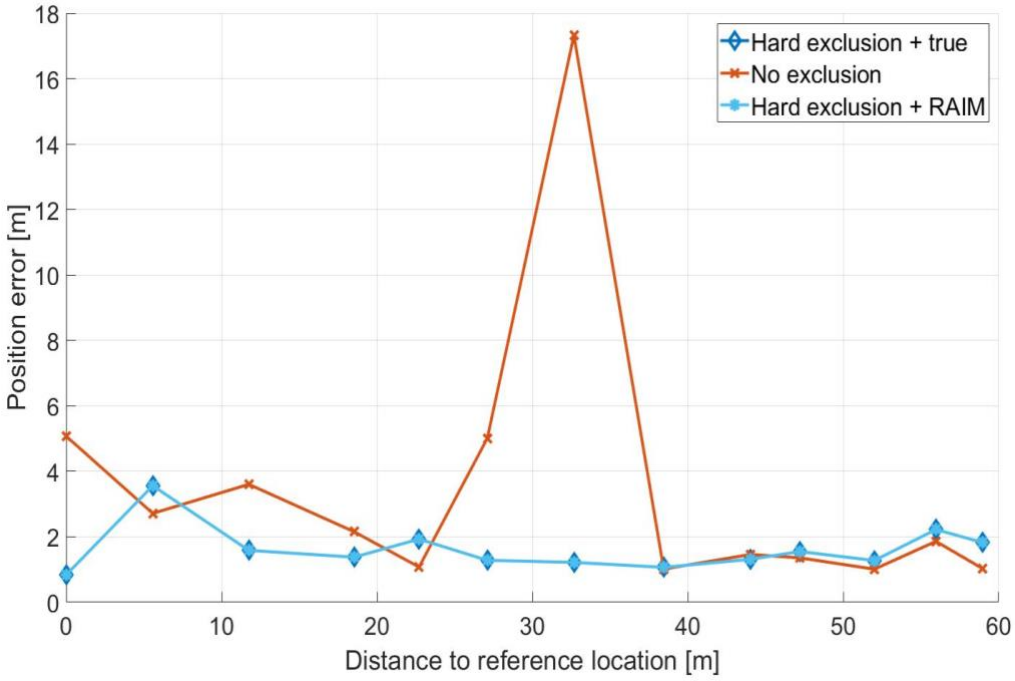

Fig. 17. Position error at each testing location for the no exclusion algorithm, the hard + RAIM algorithm, and the hard exclusion algorithm initialized with true location.

The soft exclusion algorithm also produces solutions with consistently low errors that is within the range of nominal GPS error. The uncertainty model in the soft exclusion is developed to handle building model uncertainty. But in doing that it also handles some initial position error.

The soft exclusion algorithm and RAIM algorithm produce similar results at all locations. In order to investigate and further compare the performance of both algorithms, additional data collection was conducted at a different location within the Engineering Quad (Fig. 18). Position error for both algorithms were plotted over a time period of 0.6 minute in Fig. 19. It can be seen that in this scenario, RAIM failed to exclude all the erroneous signals and results in larger position error than the soft exclusion algorithm. RAIM algorithm requires that the majority of the signals are clean, and it works best when only one corrupted signal

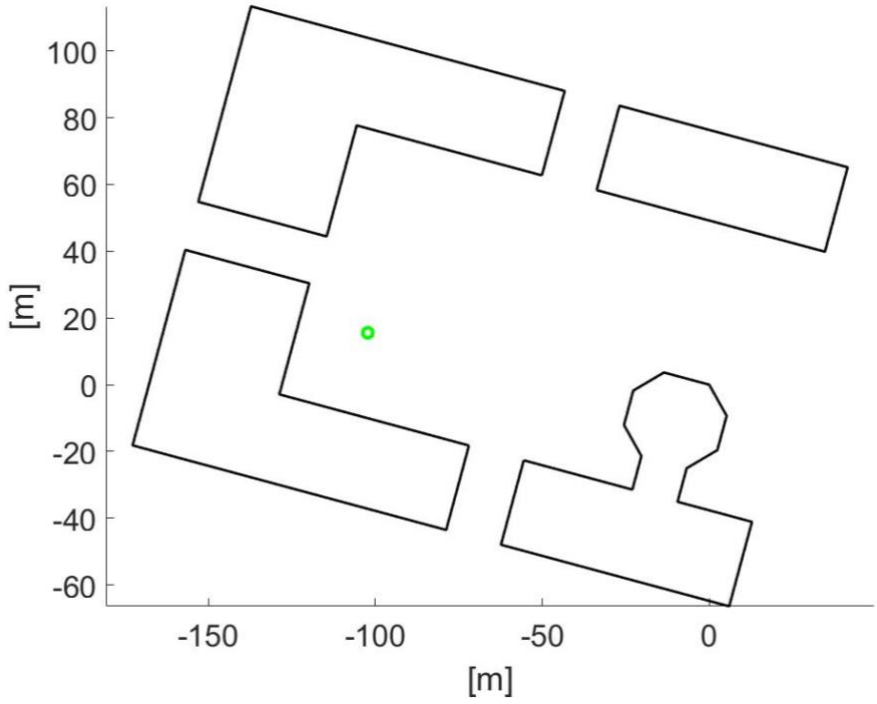

Fig. 18. Ground truth of receiver collecting data at an additional testing location.

exists among the received signals. RAIM also requires redundancy to check consistency among the signals. If there are only four signals present in a given scenario, RAIM cannot give any clear indication on whether any of the signals are corrupted by multipath. On the other hand, soft exclusion does not have either of the restrictions and can still detect multipath even in severe environments where the majority of signals are multipath or are blocked by buildings. Currently, the soft exclusion algorithm is based on a simple, uniformly distributed statistical model to simulate building uncertainty. Further analysis can be done to refine the statistical model to better capture the uncertainty in both the building model and user location, and to improve the algorithm's prediction accuracy.

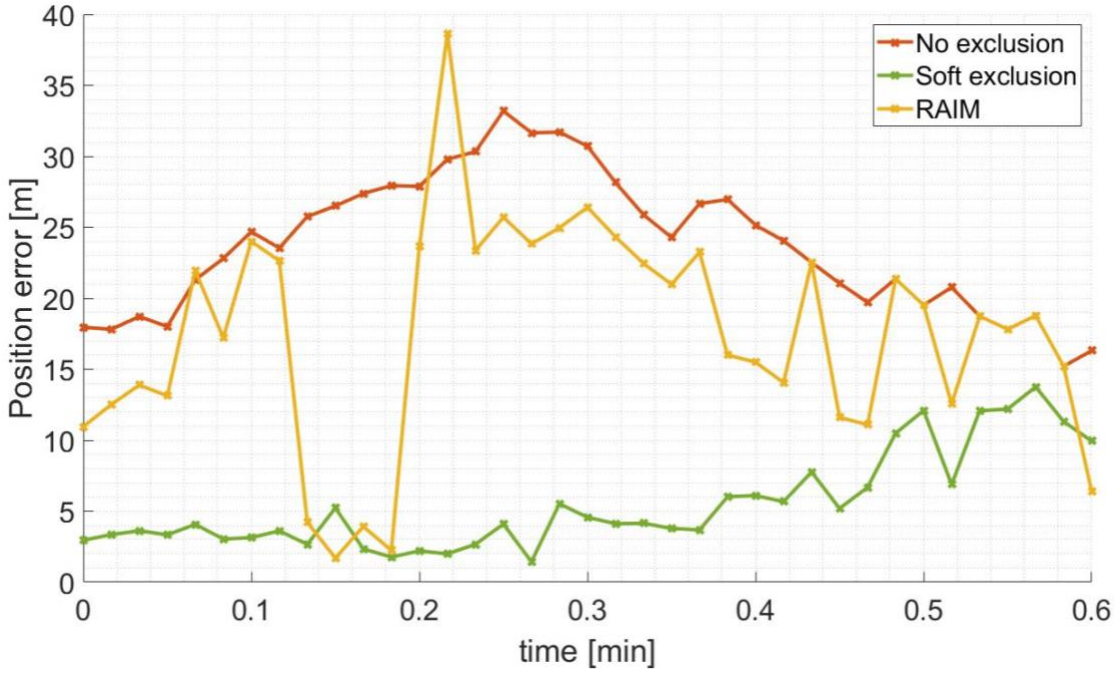

Fig. 19. Comparison of position error between the soft exclusion algorithm and RAIM at additional testing location.

4. Multi-Frequency Multipath Estimation

This chapter proposes and evaluates a multipath detection and mitigation method that uses multi-frequency correlation functions to identify, estimate, and remove multipath error from received signals. A dual frequency multipath model was developed using multipath relative delay, amplitude and phase, and the relationship of multipath delay and amplitude between two different frequencies. Multipath delay, amplitude and phase were randomly generated through simulation to evaluate the performance of the estimation algorithm.

4.1 Multipath Parameter Estimation

The auto-correlation function (ACF), $R(\tau)$, for a GNSS signal is defined in the time domain as

$$R(\tau) = \frac{1}{T_{code}} \int_0^{T_{code}} x(t)x(t-\tau)dt$$

where $x(t)$ is the PRN code and T_{code} is the period of $x(t)$. When $\tau = nT_{code}$ where $n = 0, \pm 1, \pm 2, \cdots$, the ACF takes on the maximum value of 1.

Fig. 20 shows the auto-correlation function for a typical GPS L1 C/A signal. The ACF can be approximated as a triangular function with its peak at $t = 0$, and with the base of the triangle equals to $2T_C$, where T_C is the duration of the single chip.

As shown in Fig. 20a, the ideal ACF is a triangular function. “Ideal” refers to that no precorrelation filter was applied to the signal and hence the signal used has infinite bandwidth. This produces an ACF with a sharp peak. A precorrelation filter is usually used to remove out-of-band noise and interference. But the filter also changes the shape of the

ACF and smooths out the edges, making multipath harder to distinguish. A narrower filtering bandwidth corresponds to a smoother shape of the ACF. Fig. 20b shows the filtering effect on the shape of the auto-correlation function.

Let $R_{ref}(t)$ be the standard filtered ACF with unit amplitude and with its peak at $t = 0$. Then the ACF of any received GNSS signal can be expressed as a function of $R_{ref}(t)$ corresponding to that signal's pseudorandom code shifted by signal time delay τ, scaled by signal amplitude A, and rotated by carrier phase θ. If both direct signal and reflections are present, the received signal is the superposition of all of the components with a different amplitude, delay, and phase for each component.

$$S(t) = \sum_{i=0}^{n} A_i R_{ref}(t - \tau_i) e^{j\theta_i} + n(t)$$

In the above equation, $i = 0$ represents the direct LOS component of the received signal, and $i = 1, 2, \ldots, n$ are the reflection components. $n(t)$ captures white Gaussian noise in the received signal.

Since the standard ACF $R_{ref}(t)$ is known to the receiver, we can estimate the signal parameters $\widehat{\tau_i}$, $\widehat{A_i}$, and $\widehat{\theta_i}$ by minimizing the following cost function

$$C = \int_{-T_C}^{T_C} \left(S(t) - \sum_{i=0}^{n} \widehat{A_i} R_{ref}(t - \widehat{\tau_i}) e^{j\widehat{\theta_i}} \right)^2 dt$$

If the receiver uses multiple complex correlators to generate sampling points $S(t_j)$ of the received signal at time t_j's, the cost function can be written in discrete form with m being the sample times or sample points/delay relative to τ as

$$C = \sum_{j=0}^{m} \left(S(t_j) - \sum_{i=0}^{n} \widehat{A_i} R_{ref}(t_j - \widehat{\tau_i}) e^{j\widehat{\theta_i}} \right)^2$$

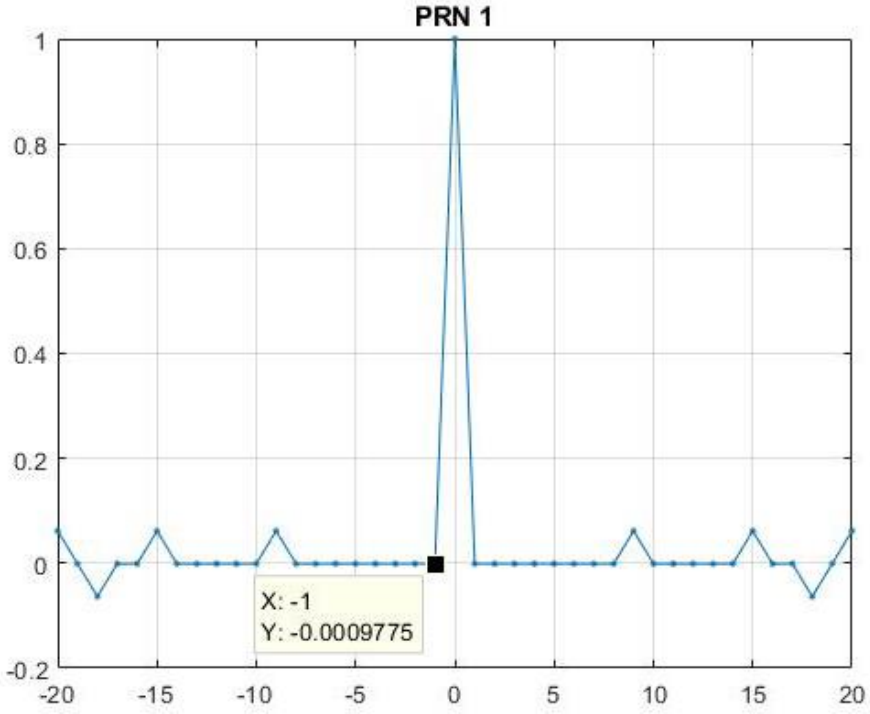

(a)

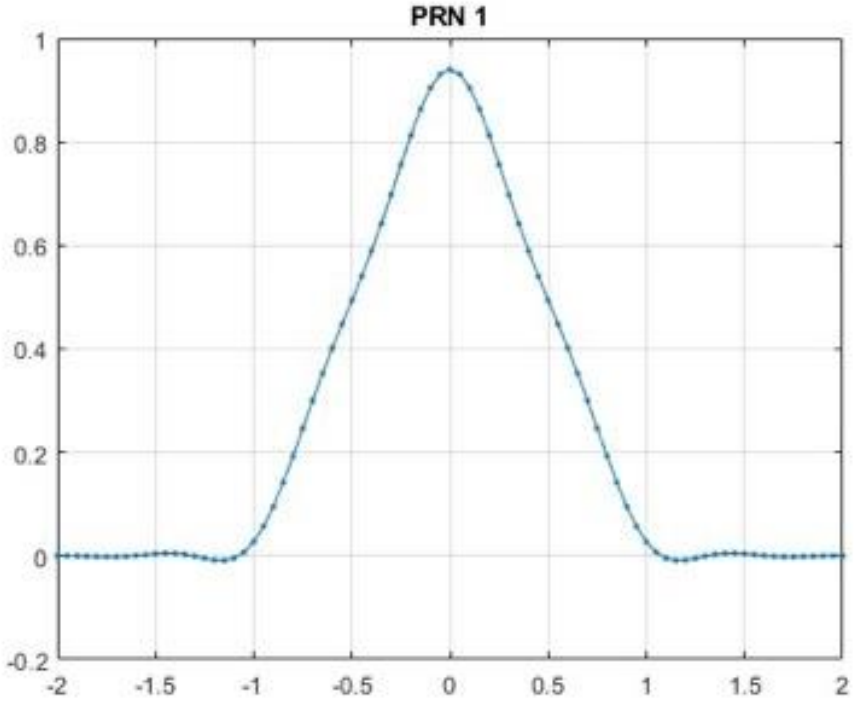

(b)

Fig. 20. (a) Auto-correlation function of GPS L1 C/A-code PRN01; (b) auto-correlation function of PRN01 after passing through an 8MHz low-pass filter.

4.2 Multi-Frequency Multipath Parameter Estimation

The U.S. government is in the process of adding new navigation signals to the GPS constellation. In addition to the GPS L1 C/A legacy signal, two new civil signals, L2C and L5, are available on certain GPS satellites. These three civil signals are broadcasting on different radio frequencies: L1 C/A is broadcasting on a central frequency of 1575.42 MHz, L2C on 1227.6 MHz, and L5 on 1176.45 MHz. The diversity in frequency provides additional information that can help in estimating multipath parameters.

If a satellite is broadcasting on multiple frequencies, the direct LOS signal path and multipath signal path are nearly identical on different frequencies. Therefore, multipath path delays are the same across different frequencies. Similarly, since reflectivity does not vary much across different GNSS frequency bands, the relative amplitude ratio between multipath and LOS component stays the same across different frequencies as well. In term of phase angle, since the wavelength of each frequency signal is different, signal traveling through the same path will likely end up with different phase angle and therefore cause different distortion in ACF. Fig. 21 demonstrates how different phase angles affect the shape of ACF. In a typical GNSS receiver, a received signal is demodulated into I (in-phase) and Q (quadrature) components. Fig. 21 shows the correlator outputs for both I-channel and Q-

channel. The relationship of multipath delay, amplitude, and phase across different frequencies can be used in multipath parameter estimation.

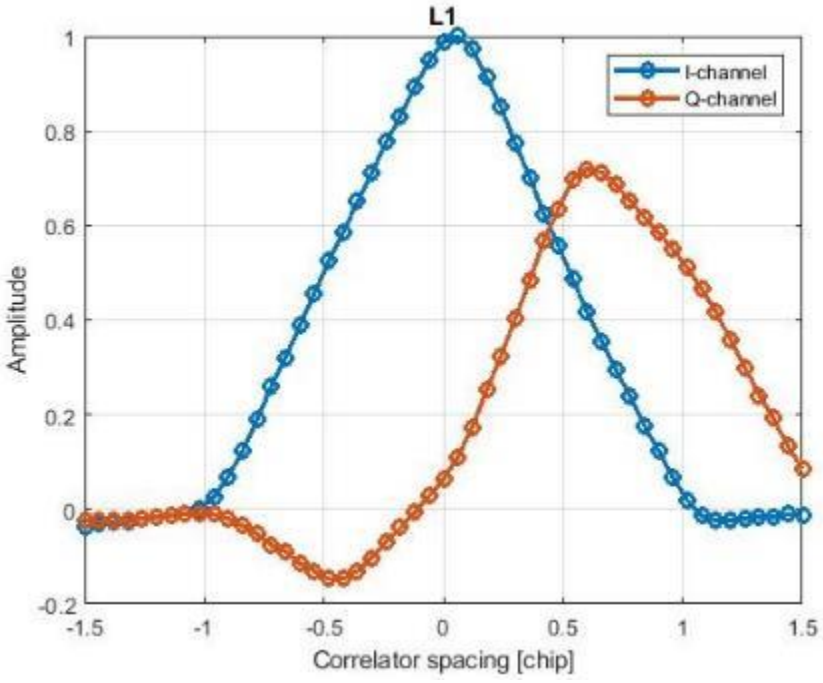

(a)

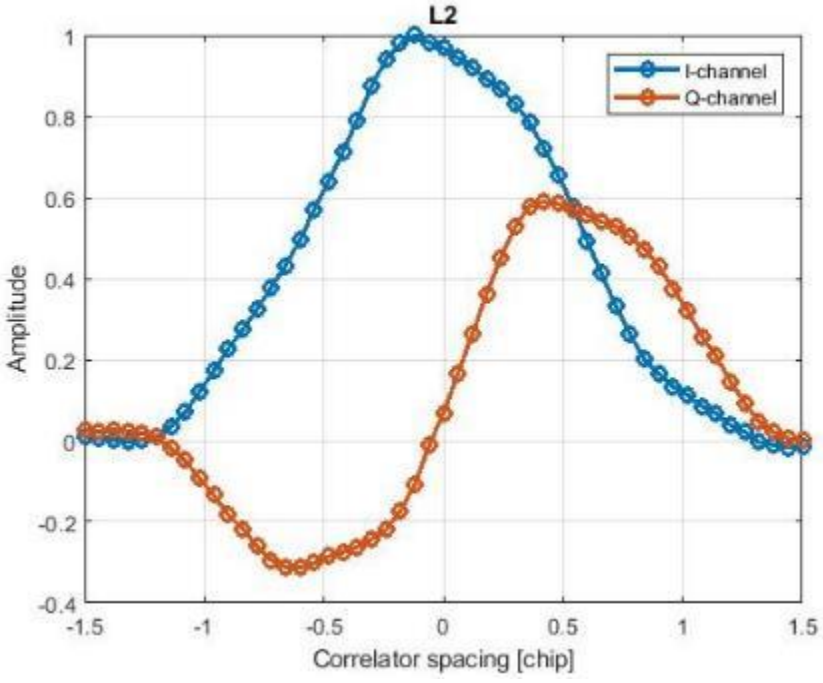

(b)

Fig. 21. (a) Auto-correlation function of a GPS L1 signal; (b) auto-correlation function of the corresponding GPS L2 signal.

For dual frequency signals, mathematically, these relationships can be expressed as following:

$$\tau_i^p - \tau_0^p = \tau_i^q - \tau_0^q$$

$$\tau_i^k - \tau_0^k > 0, \qquad \text{for } k = p, q$$

$$\frac{A_i^p}{A_0^p} = \frac{A_i^q}{A_0^q}$$

$$0 < \frac{A_i^k}{A_0^k} < 1, \qquad \text{for } k = p,$$

where $i = 1, \dots, n$, is the index of the multipath reflection and p and q can take on values of L1, L2C, or L5. The reflected signal always travels a longer path than the direct LOS signal and therefore is always delayed with respect to the direct signal. It is assumed that the reflected signal is always weaker than the LOS signal and therefore the amplitude ratio of the reflected signal to the direct signal is assumed to be always less than 1.

The corresponding cost function for dual frequency estimation can be expressed as the weighted sum of the individual cost function as defined in 3.2 with weights on the signal on frequency p, q given by w_p and w_q, respectively.

$$C = w_p C_p + w_q C_q$$

4.3 Change of Variables

An optimization problem with non-linear constraints to solve the multipath parameters can be formulated as below:

$$\min_{\widehat{\tau_i}, \widehat{A_i}, \widehat{\theta_i}} w_p C_p + w_q C_q$$

$$\tau_i^p - \tau_0^p = \tau_i^q - \tau_0^q$$

$$\tau_i^k - \tau_0^k > 0, \qquad \text{for } k = p, q$$

$$\frac{A_i^p}{A_0^p} = \frac{A_i^q}{A_0^q}, \qquad \text{for } i = 1, \dots, n$$

$$0 < \frac{A_i^k}{A_0^k} < 1, \qquad \text{for } k = p, q$$

Theoretically, solving the above optimization problem should give us the correct answer. But practically, since this is not a convex problem, it is not guaranteed that the global optimal solution will be found. Additionally, since the complex exponential is a periodic function with its derivatives also periodic functions, and with the phase angle taking on values from $-\infty$ to ∞, it is difficult for any optimization algorithm to find the global optimal on θ_i's. Therefore, a better formulation of the optimization problem is needed to improve the performance of the optimization algorithm to find global optimal solutions.

Since θ_i's are the variables that are causing problems, we want to replace these variables with non-cyclical variables. First, by expanding the complex exponentials, we can rewrite them as follow:

$$e^{j\theta_i} = cos\theta_i + \boldsymbol{j} sin\theta_i$$

And we can rewrite the ACF of a received signal on frequency k as

$$S^k(t) = \sum_{i=0}^{n} A_i^k R_{ref}^k\left(t - \tau_i^k\right)(cos\theta_i^k + \boldsymbol{j} sin\theta_i^k)$$

$$= \sum_{i=0}^{n} R_{ref}^k\left(t - \tau_i^k\right)(A_i^k cos\theta_i^k + \boldsymbol{j} A_i^k sin\theta_i^k)$$

Let $A_{i,I}^k = A_i^k cos\theta_i^k$ and $A_{i,Q}^k = A_i^k sin\theta_i^k$,

$$S^k(t) = \sum_{i=0}^{n} R_{ref}^k\left(t - \tau_i^k\right)(A_{i,I}^k + \boldsymbol{j} A_{i,Q}^k)$$

where ${A_i^k}^2 = {A_{i,I}^k}^2 + {A_{i,Q}^k}^2$. And the cost function becomes

$$C^k = \sum_{j=0}^{m} \left(S^k(t_j) - \sum_{i=0}^{n} \left(\widehat{A_{i,I}^k} R_{ref}^k(t_j - \widehat{\tau_i^k}) + \boldsymbol{j}\, \widehat{A_{i,Q}^k} R_{ref}^k(t_j - \widehat{\tau_i^k}) \right) \right)^2$$

The constraints on τ_i's stay the same, but the constraints on amplitudes need to be rewritten as

$$\frac{{A_{i,I}^p}^2 + {A_{i,Q}^p}^2}{{A_{0,I}^p}^2 + {A_{0,Q}^p}^2} = \frac{{A_{i,I}^q}^2 + {A_{i,Q}^q}^2}{{A_{0,I}^q}^2 + {A_{0,Q}^q}^2}$$

In summary, the new optimization problem after change of variables is as follow

$$\min_{\widehat{\tau_i}, \widehat{A_{i,I}}, \widehat{A_{i,Q}}} w_p C_p + w_q C_q$$

$$\tau_i^p - \tau_0^p = \tau_i^q - \tau_0^q$$

$$\tau_i^k - \tau_0^k > 0, \qquad \text{for } k = p, q$$

$$\frac{{A_{i,I}^p}^2 + {A_{i,Q}^p}^2}{{A_{0,I}^p}^2 + {A_{0,Q}^p}^2} = \frac{{A_{i,I}^q}^2 + {A_{i,Q}^q}^2}{{A_{0,I}^q}^2 + {A_{0,Q}^q}^2}, \qquad \text{for } i = 1, \dots, n$$

For the rest of this chapter, we will refer to the formulation before change of variables as the exponential formulation and the one after change of variables as the IQ formulation.

4.4 Simulation Results

Simulations were set up to evaluate the performance of dual frequency multipath estimation and mitigation. L1 and L2C signals were selected for simulation because these two civil signals have the same chipping rate and are have similar performance under multipath conditions. Due to a limitation of simulation, the real L2C pseudorandom code was not available to be implemented. Instead, the corresponding L1 C/A code from the same satellite

was used to simulate L2C signal. This also allows us to single out and observe the effect of multipath parameters on the estimation problem.

Even though the estimation problem that was set up in the previous section can be used for any number of multipath components, for the purpose of evaluating the algorithm's performance, the assumption of having only one dominant multipath in a received signal was made.

Several design parameters were chosen to set up the simulation environment. Filtering bandwidth affects the shape of the correlation function. A lower bandwidth can smooth out the distortion of multipath and make it less distinguishable. A filtering bandwidth of 8 MHz was chosen because this value is achievable for GNSS receivers and still retains most of the distortion caused by multipath.

More than one standard pair of early and late correlators are needed to estimate the shape of the correlation function. The more correlators are used, the better the approximation will be. But this benefit diminishes as the number of correlators increases. 50 correlators were chosen on the interval $[-1.5, 1.5]$ chips to capture the trailing effect of multipath and the case when the receiver is tracking the NLOS signal instead of LOS.

Another design parameter to consider was integration time. Since longer integration time is helpful in reducing noise, an integration time of 20 milliseconds was chosen to enhance performance under noise while still remain within the range of practical values. Coherent integration was used in simulation because navigation data were not simulated. For real signal with navigation messages, bit synchronization would need to be performed before implementing the 20-millisecond integration time.

A single multipath signal with randomly generated delay, amplitude ratio, and phase was simulated and added to the LOS signal. White Gaussian noise was added to provide a simulated incoming signal with C/N_0 of 45 dB-Hz, which is the typical C/N_0 value under nominal conditions. Lower C/N_0 values result in more error in estimation because noise distort the correlation function and makes the distortion caused by multipath less noticeable. The multipath delay was chosen from a uniform distribution between $(0, 2]$ chips. The amplitude ratio was chosen from a uniform distribution between $(0, 0.9]$. And the phase angle was chosen from a uniform distribution between $[0, 2\pi]$ radians. Multipath estimation was then performed on the received ACF with multipath and the estimated multipath component of ACF was removed from the received ACF. A pair of early and late correlator with spacing of 1 chip was used to obtain range measurement from the ACF after it was corrected for multipath. A spacing of one-chip was used because it is the standard correlator spacing used in most GNSS receivers and the benefit of multipath estimation can be observed fully without considering the multipath mitigation effect of narrower correlator spacing.

Simulation results are presented in Fig. 22 for both single frequency multipath estimation and dual frequency multipath estimation, as well as for both the exponential formulation and the IQ formulation. First of all, it can be seen from Table III to VI that both single and dual frequency mitigation reduced multipath range errors significantly in terms of both root-mean-squared (rms) errors and worse case errors. But looking at Table III and IV, we see that dual frequency under exponential formulation did not produce any obvious improvement on rms errors or worse case errors over single frequency mitigation. On the other hand, comparing Table III and V and Table IV and VI shows

that under IQ formulation, dual frequency shows more obvious improvement on both rms and worse case errors over single frequency mitigation. This is because under exponential formulation, the complexity of adding an additional signal added significant burden on finding the global optimal solution due to the cyclical nature of the partial derivative of the cost function with respect to phase angles. Moreover, comparing Table III and V shows that both single and dual frequency mitigation under IQ formulation performs better than their corresponding exponential formulation, which further demonstrated that IQ formulation provides greater advantages in finding the global optimal solution.

TABLE III. RMS ERROR FOR SINGLE AND DUAL FREQUENCY MITIGATION WITH EXPONENTIAL FORMULATION (C/N_0 = 45 dB-Hz)

Algorithms	**L1 multipath error [m]**	**L2 multipath error [m]**
No mitigation	8.6566	7.7729
Single frequency mitigation	5.0476	4.8385
Dual frequency mitigation	5.1229	4.6187

TABLE IV. WORST CASE ERROR FOR SINGLE AND DUAL FREQUENCY MITIGATION WITH EXPONENTIAL FORMULATION (C/N_0 = 45 dB-Hz)

Algorithms	**L1 multipath error [m]**	**L2 multipath error [m]**
No mitigation	28.0589	27.4729
Single frequency mitigation	11.1392	11.2101
Dual frequency mitigation	11.1465	11.2091

TABLE V. RMS ERROR FOR SINGLE AND DUAL FREQUENCY MITIGATION WITH IQ FORMULATION (C/N_0 = 45 dB-Hz)

Algorithms	L1 multipath error [m]	L2 multipath error [m]
No mitigation	8.6566	7.7729
Single frequency mitigation	3.4787	4.3292
Dual frequency mitigation	3.3823	3.8846

TABLE VI. WORST CASE ERROR FOR SINGLE AND DUAL FREQUENCY MITIGATION WITH IQ FORMULATION (C/N_0 = 45 dB-Hz)

Algorithms	L1 multipath error [m]	L2 multipath error [m]
No mitigation	28.0589	27.4729
Single frequency mitigation	7.8265	11.8854
Dual frequency mitigation	7.7295	7.9334

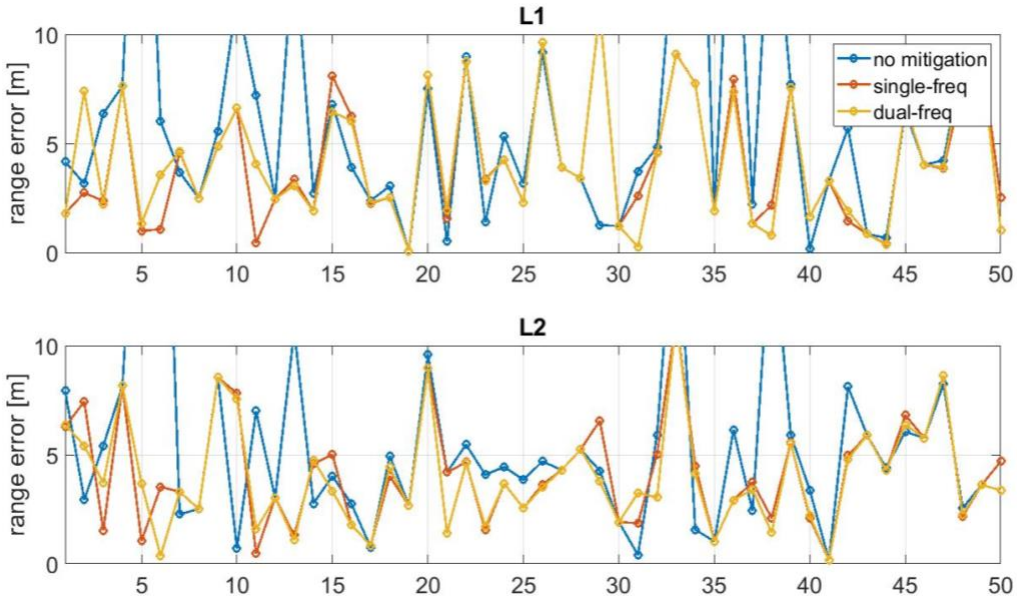

(a)

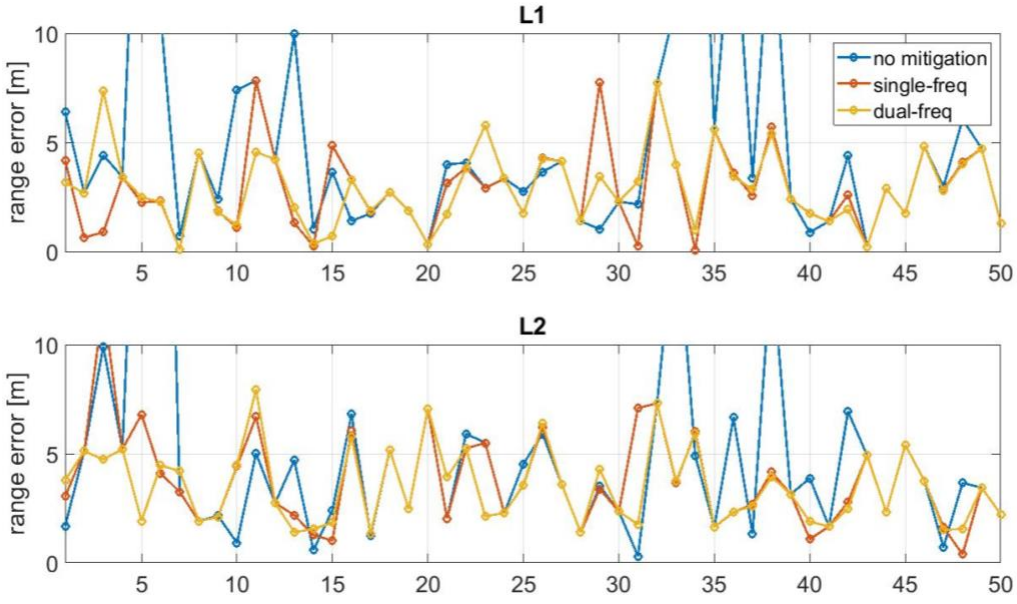

(b)

Fig. 22. (a) Multipath range errors at 50 different simulation runs with 45dB-Hz C/N_0 after single and dual frequency mitigation for exponential formulation; (b) Multipath range errors at 50 different simulation runs with 45dB-Hz C/N_0 after single and dual frequency mitigation for IQ formulation.

In conclusion, results from both single frequency and dual frequency mitigation suggest that IQ-formulation achieves better convergence to global optimal solution. Under IQ-formulation, dual frequency mitigation can provide a tighter bound on worst case multipath error than single frequency mitigation.

5. Three-Dimensional Map Generation Using GNSS Signals

This chapter describes and examines three probability-based voting algorithms to generate three-dimensional (3D) occupancy map using GNSS signals. A 3D occupancy map is a way to represent a 3D environment by evenly discretizing the environment into 3D voxels, each having an associated occupancy value that describes the probability of the presence of an obstacle at that voxel location in the environment. The map generation algorithms are designed to only require basic data (user position, satellite position, signal-to-noise ratio) that are available from most Android smartphones allowing them to produce meaningful results solely based on crowdsourced data. The generation starts by creating rays from the user location to each received GNSS satellite. The basic concept with each algorithm is to develop a probability model to assign the probability that the signal has a direct Line of Sight (LOS) to each of the satellite signals according to their signal-to-noise ratio (SNR) measurements. The map generation algorithms then use these GNSS rays and the probability of LOS to infer the 3D environment. Simulations were conducted to validate each of the three map generation algorithms. GNSS sensor data collected from Uber driver's smartphones were used to evaluate and compare the performance of each algorithm.

5.1 LOS and NLOS Classification

Fundamental to each algorithm is classifying whether the signal is LOS or NLOS. As we may not have many metrics from the receiver to aid in this determination, a simple model

to predict the probability of LOS for each received GNSS signal based on the statistical model of SNR described in [16] was used. The model assumes that LOS signals follow the Rician distribution and the NLOS signals are log-normal distributed. Detail explanation of how these statistical models were developed and how the parameters were chosen can be found in [22] and [23]. Fig. 23 shows the probability density function of the LOS and NLOS distributions, given by f_{LOS} and f_{NLOS}, respectively. Given a SNR measurement, probability of LOS can be calculated using the likelihood ratio as follow, assuming an equal a priori probability of LOS and NLOS:

$$\text{Prob}(\text{LOS}(x)) = \frac{f_{LOS}(x)/f_{NLOS}(x)}{1 + f_{LOS}(x)/f_{NLOS}(x)}$$

Fig. 24 shows all the GNSS rays associated with a single user location using real GNSS data from an Uber driver's smartphone. Probability of LOS are color-coded with red, yellow, and green representing low, medium, and high probability of LOS given the recorded SNR values, respectively. It can be seen from Fig. 24 that the red rays and most of the yellow rays were in fact blocked by buildings. Rays with medium probability of LOS are likely the ones with both LOS and NLOS components and are not very informative for map inference. Therefore, only rays with high or low probability of LOS are used in map generation algorithms.

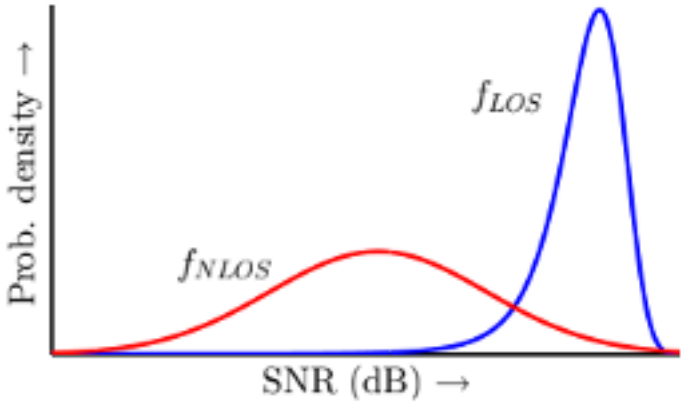

(a)

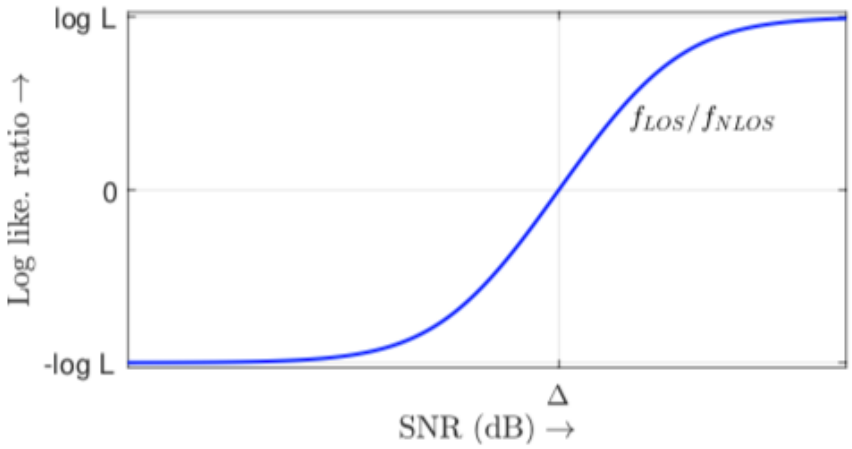

(b)

Fig. 23. (a) LOS and NLOS probability distributions for SNR measurements. (b) LOS/NLOS log likelihood ratio as a function of SNR.

5.2 Map Generation Algorithms

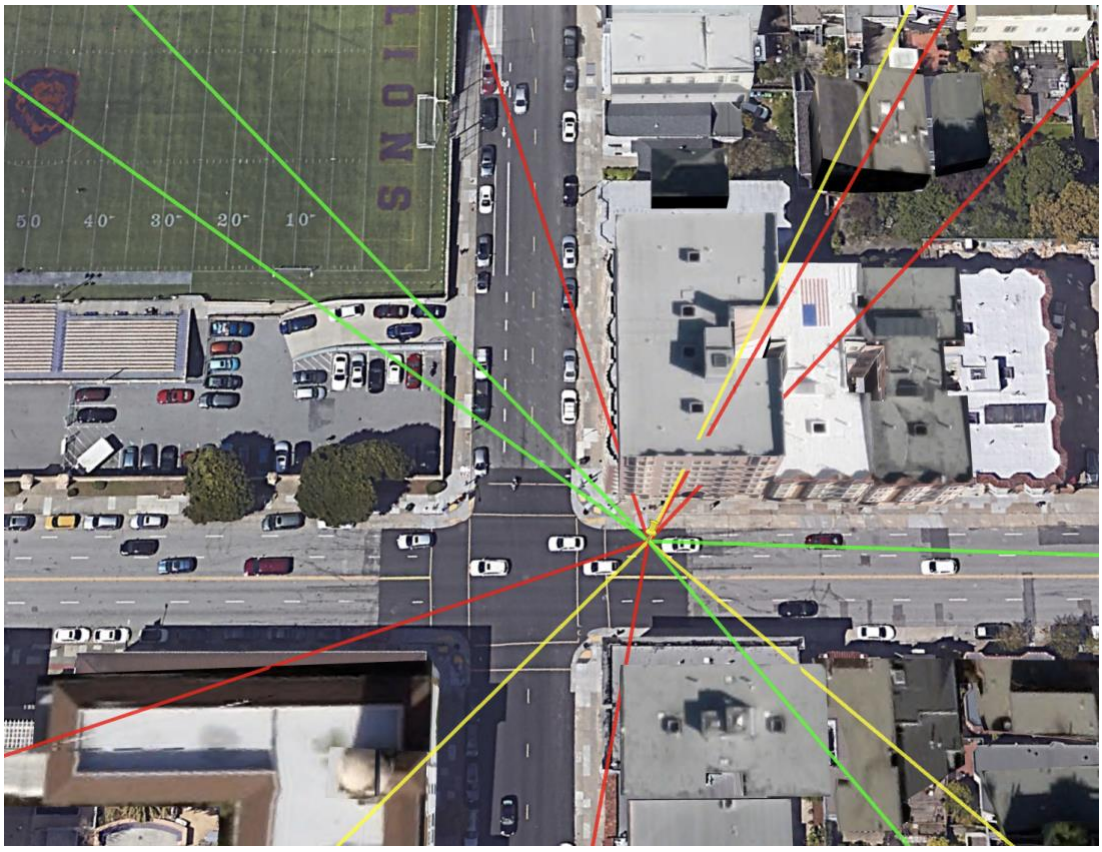

Fig. 24. GNSS rays associated with a single user location, plotted in Google Earth. Red: Prob(LOS) < 0.4; Yellow: 0.4 < Prob(LOS) < 0.8; Green: Prob(LOS) > 0.8.

Three map generation algorithms were implemented and evaluated – the negative voting algorithm, the positive voting algorithm, and the combined voting algorithm. All three algorithms are probability-based voting algorithms. The 3D region to be mapped was first discretized into small 3D voxels with a desired resolution. Each voxel has an associated probability of occupancy to indicate how likely the voxel is occupied. The occupancy probabilities can be initialized based on a coarse map of the region if such information is available. But in this chapter, we assume no a priori information of the region is available, and the occupancy probabilities are initialized based on the map generation algorithm used. The map generation algorithm takes in GNSS rays that pass through the

3D region of interest and assigns votes to alter the probability of occupancy for the associated voxels according to the probability of LOS of each ray.

5.2.1 Negative Voting Algorithm

The negative voting algorithm works by using measurements to eliminate regions that are unoccupied (i.e. not blocked/not a building). Intuitively, it is like ice carving. All the voxels in the 3D region are initialized with probability of occupancy equals to 1, which means that the entire 3D region is initialized as completely occupied. And for each of the LOS rays, all the voxels along the path of ray are carved out by decreasing the probability of occupancy associated with those voxels. The probabilities of occupancy for the voxels that the LOS ray passes through are decreased by the probability of LOS of the LOS ray.

5.2.2 Positive Voting Algorithm

The positive voting algorithm uses the probability of NLOS to determine which voxels are occupied. Instead of voting down the probability of occupancy using LOS rays, the positive voting algorithm uses NLOS rays to predict the voxels that are likely to be occupied. The algorithm initializes the probability of occupancy for all voxels to 0. The algorithm can be broken down into three major steps. The first step is to project all the NLOS rays onto the ground plane to create a 2D density map of the region of interest. For each NLOS ray, the probability of occupancy for the voxels on the ground plane that the projected NLOS ray passes through were updated based on the probability of NLOS calculated from the associated SNR value. The second step is to identify the building footprints in the region using a threshold value or a clustering algorithm. The final step is

to reconstruct the 3D buildings using these footprints and the NLOS rays. A detailed description of the steps can be found in [15]. The positive voting algorithm implemented in this chapter is a slight variation of the algorithm described in [15]. In the first step, instead of calculating probability of NLOS using the mean value and the range of SNR measurements, the statistical model described in Section 5.2 was used. And in the second step, for simplicity, a single threshold value was used to determine building footprints.

5.2.3 Combined Voting Algorithm

The third and final algorithm implemented is the combined voting algorithm which uses both LOS and NLOS rays to assign probability of occupancy for each voxel that the rays pass through. This algorithm initializes all voxels with probability of occupancy equaling to 0.5. Then the same method as described in 5.3.2 is used to generate the 2D density map using NLOS rays and to identify building footprints. LOS rays are not used in the footprint generation step. Finally, both LOS and NLOS rays are used to increase or decrease the probability of occupancy of the voxels according to the probability of LOS for each ray. And the method to update probability of occupancy is the same as the methods described in negative voting and positive voting algorithms.

5.3 Simulation Results

Simulations were conducted to validate each of the three map generation algorithms. GNSS rays were simulated by randomly generating points on the ground of the 3D space, and then randomly generating unit vectors with positive z-components. Three rectangles of different size and volume were generated to resemble 3D buildings (Fig. 25).

Simulations assume perfect knowledge of the rays so probability of LOS for LOS rays was set to 1 and probability of LOS for NLOS rays was set to 0.

Fig. 26 shows simulation result for the negative voting algorithm. The yellow boxes represent the occupied voxels from simulation and the grey boxes represent the truth of three rectangular buildings. There is discrepancy at the top of the buildings because the top of the building is not fully observable by rays originated from the ground to the sky. This unobservability problem results in pyramid-shaped rooftops for buildings generated using negative voting algorithm. If the boundaries of the 3D space were expanded, the unobservability region at the top of the buildings will be reduced. And if the boundaries of the 3D space were expanded to infinity, the unobservability problem will be completely eliminated. Fig. 27 shows simulation result for the positive voting algorithm. It can be seen that the algorithm generated perfect building footprints in simulation, but the smallest building cannot be fully constructed in 3D. This is because the rays were generated from a uniform distribution and the smallest building has the least number of rays passing through it. Therefore, the smallest building did not receive enough votes to construct itself fully. However, if more NLOS rays were generated, eventually, the

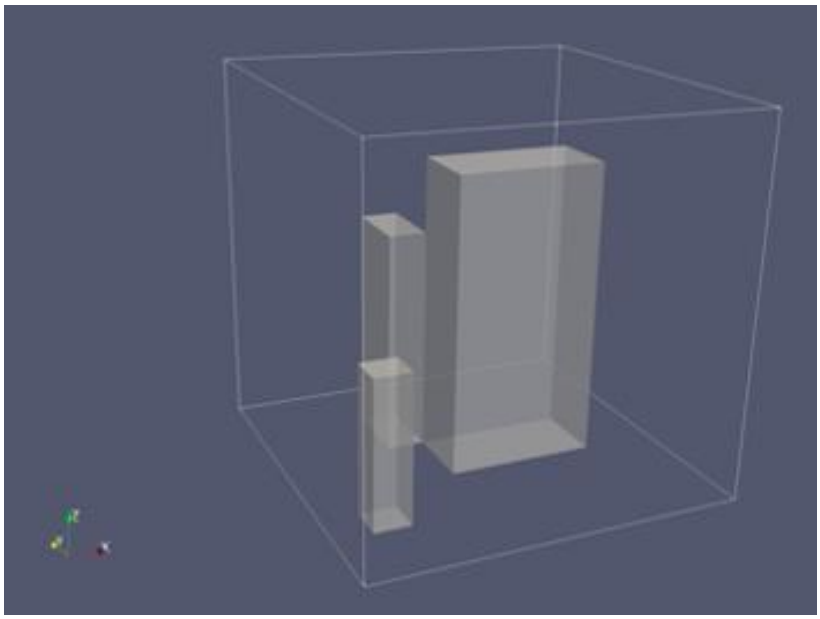

Fig. 25. Simulation scenario with three rectangles representing three 3D buildings.

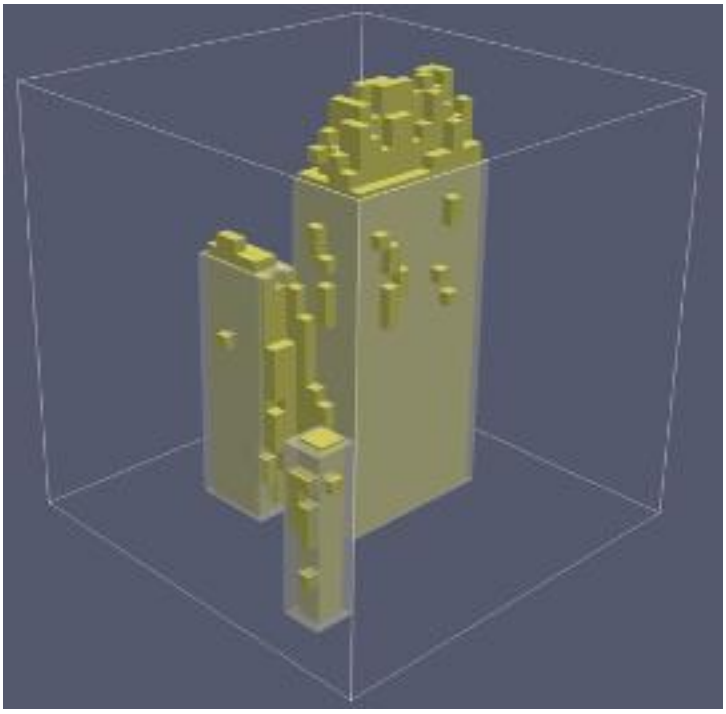

Fig. 26. Simulation result for negative voting algorithm with grey boxes representing the truth.

probability of occupancy would saturate for the larger buildings, and enough rays would pass through the smallest building so that the smallest building will be constructed

correctly and fully. Fig. 28 shows the simulation result for the combined voting algorithm. The combined voting algorithm was able to construct the smallest building

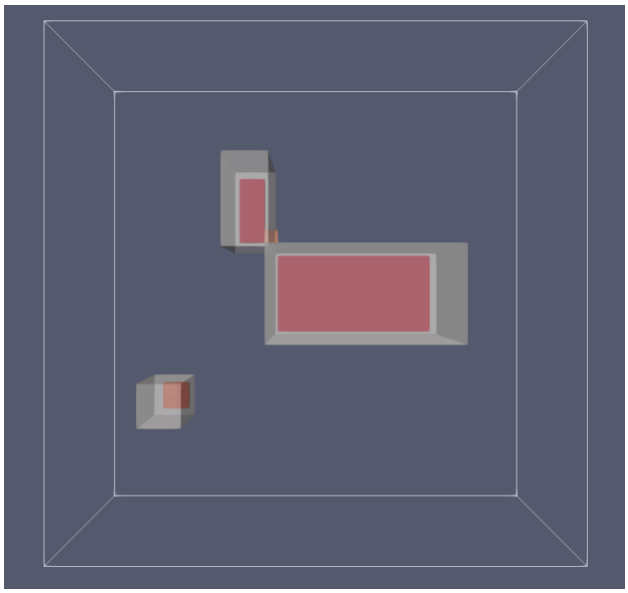

(a)

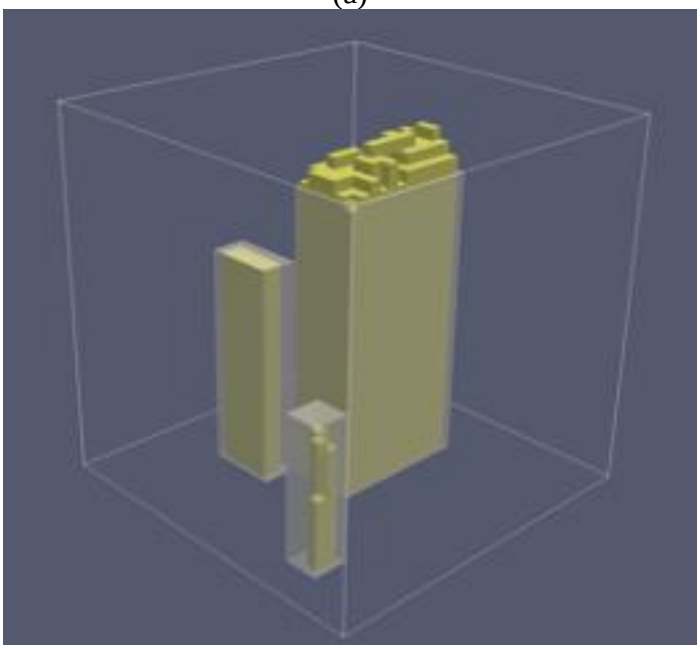

(b)

Fig. 27. (a) 2D building footprints for positive voting algorithm. (b) Simulation result for positive voting algorithm.

fully, and it eliminated the unobservability problem on top of buildings in the negative voting algorithm.

5.4 Experimental Results

GNSS sensor data were collected from Uber drivers' smartphones to further validate the algorithms and to compare performance. Validation was conducted on data from a region of interest in north San Francisco near Fisherman's Wharf (Fig. 29). This region has two tall buildings in the middle. Each of the buildings is about 60 meters tall. This region was chosen because the two tall buildings provide distinct features for the algorithms to model and will generate strong multipath signals that may provide insightful information on the performance of different algorithms.

Fig. 29 also shows a small sample of the location data collected from Uber drivers' smartphones. For each user location, the smartphone also gives the satellite positions and SNR measurements for all the received satellite signals that are associated with that user location, and calculates horizontal accuracy based on Horizontal Dilution of Precision (HDOP). Location data with horizontal accuracy greater than 5 meters were discarded to reduce mapping error caused by inaccurate user locations. The SNR measurements were used to calculate the probability of LOS for each received signal. And to reduce misclassification of LOS and NLOS signals, only signals with probability of LOS greater than 0.8 (classified as LOS) or lower than 0.4 (classified as NLOS) were used in the algorithms to generate 3D maps.

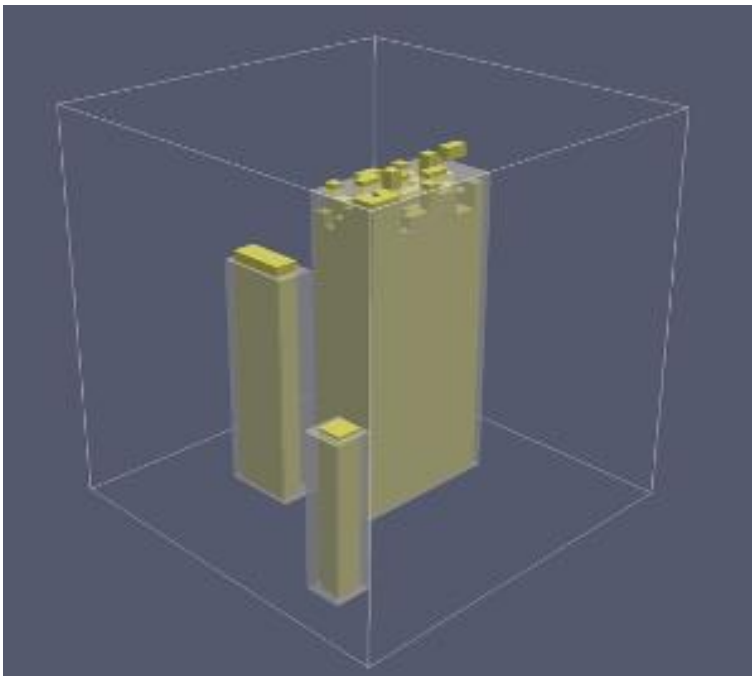

Fig. 28. Simulation result for combined voting algorithm.

Fig. 29. Region of interested in north San Francisco with boundaries marked out in white. Blue dots are user locations with horizontal accuracy lower than 5 meters and red dots are locations with horizontal accuracy greater than 5 meters.

Fig. 30 shows the experimental result for negative voting algorithm. The grey boxes are a coarse estimate of the true location and size of all the major buildings in the region of interest. These coarse estimates of truth were obtained from Google Earth. It can be seen that the two tall buildings in the middle of the region were completely and mistakenly carved out by algorithm. This is due to LOS / NLOS classification error. Strong NLOS signals reflected by the two tall buildings were misclassified as LOS and therefore carved away part of the building. With enough misclassification of rays, the buildings will eventually be completely carved away, and the negative voting algorithm cannot recover from the elimination.

Fig. 31 shows the experimental result for positive voting algorithm. The 2D density map is overlaid on top of the top view of the region of interest in Fig. 31a. Darker

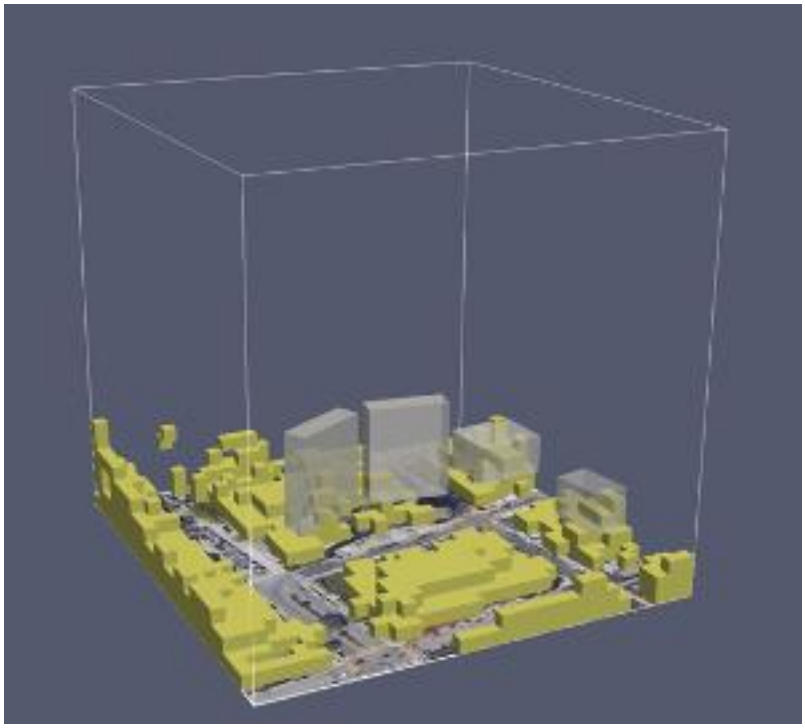

Fig. 30. Experimental result for negative voting algorithm.

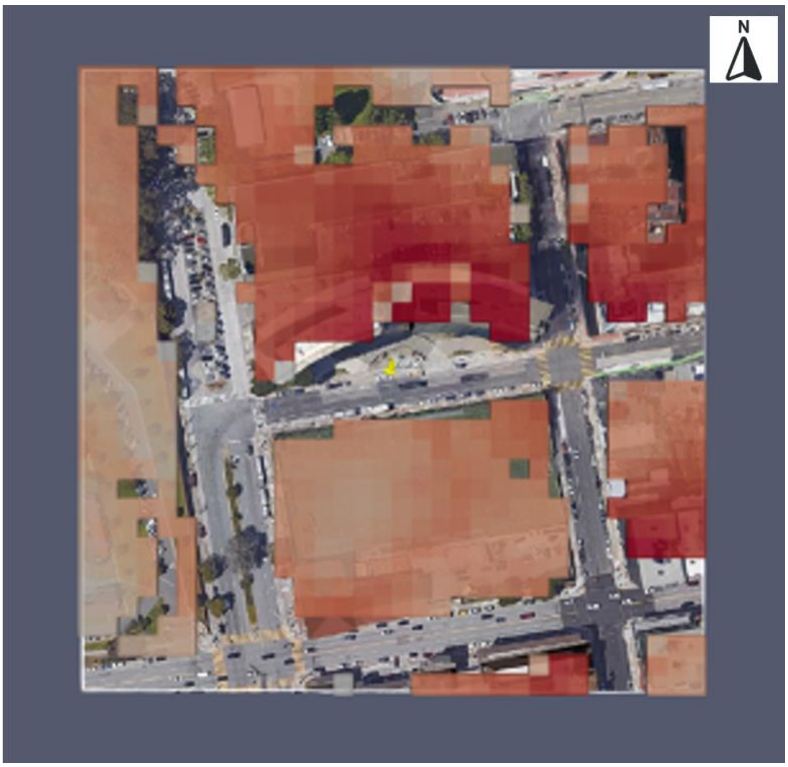

(a)

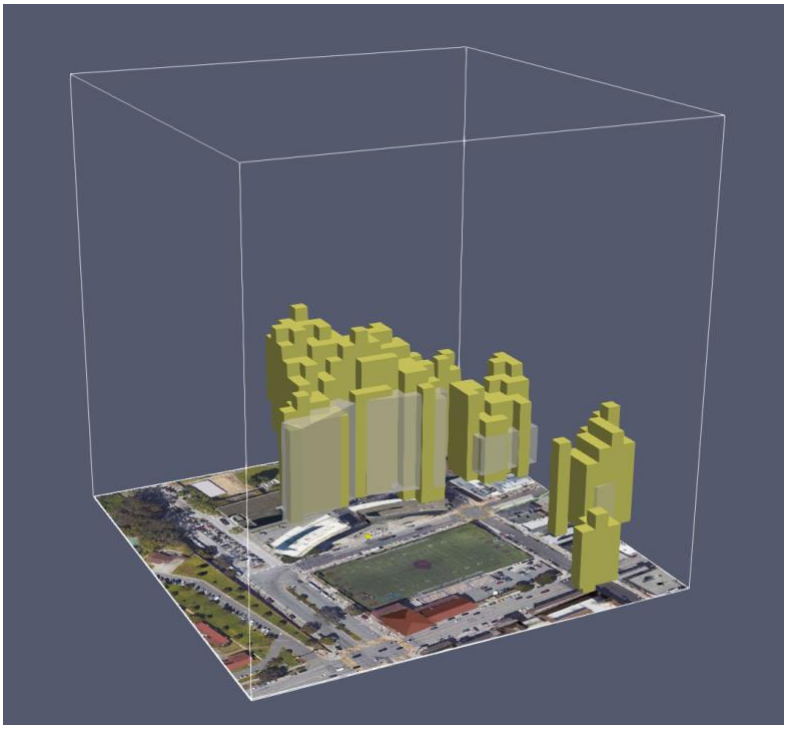

(b)

Fig. 31. (a) 2D density map overlaid on the top view of the region of interest for positive voting algorithm; (b) Experimental result for positive voting algorithm.

red in Fig. 31a represents regions with higher density. Therefore, darker red regions are likely where all the buildings reside. Fig. 31a shows that the algorithm can roughly identify the location of all the buildings in the region but cannot correctly identify the exact shape of the building footprint, especially for the two buildings in the center of the region. The inaccurate footprint is then used on the 3D construction step resulting in the error in the generated map. The reason that the algorithm cannot identify the correct footprint is that the street near the north boundary of the region is a dead-end street and therefore has very few driver location data available. This caused unobservability to the north of the buildings. Moreover, this region of interest is not flat but rather sits on a hill with the north side of the region lower than the south. To the north of the two tall buildings in the center is a platform that is higher than ground level. But since the algorithm assumes level ground in generating 2D density map, even though it was able to detect the platform to the north of the two buildings that is higher than the ground level, it was unable to distinguish it from the two tall buildings. This caused the building footprint in the center to be inaccurate and much larger than the actual buildings footprint.

Fig. 32 shows the experimental result of the combined voting algorithm. This algorithm was able to reconstruct the majority part of the two tall buildings in the middle. It shows much greater resiliency to classification error than the negative voting algorithm and resolved the unobservability issue caused by insufficient data and level ground assumption in the positive voting algorithm. With NLOS rays and the positive votes to offset the decrease in probability of occupancy caused by false LOS rays, the combined algorithm restored the central buildings that were originally carved away by the negative voting algorithm. And the LOS rays also helped offset the error caused by inaccurate

building footprint by carving out the part of building built up by the positive voting algorithm based on an inaccurate footprint.

In conclusion, the combined voting algorithm was able to leverage the strengths of the negative and positive voting algorithms and also to offset some of the weaknesses in each algorithm. Therefore, among the three map generation algorithms, the combined algorithm is the least sensitive to noise in measurements and error in classification of LOS and NLOS.

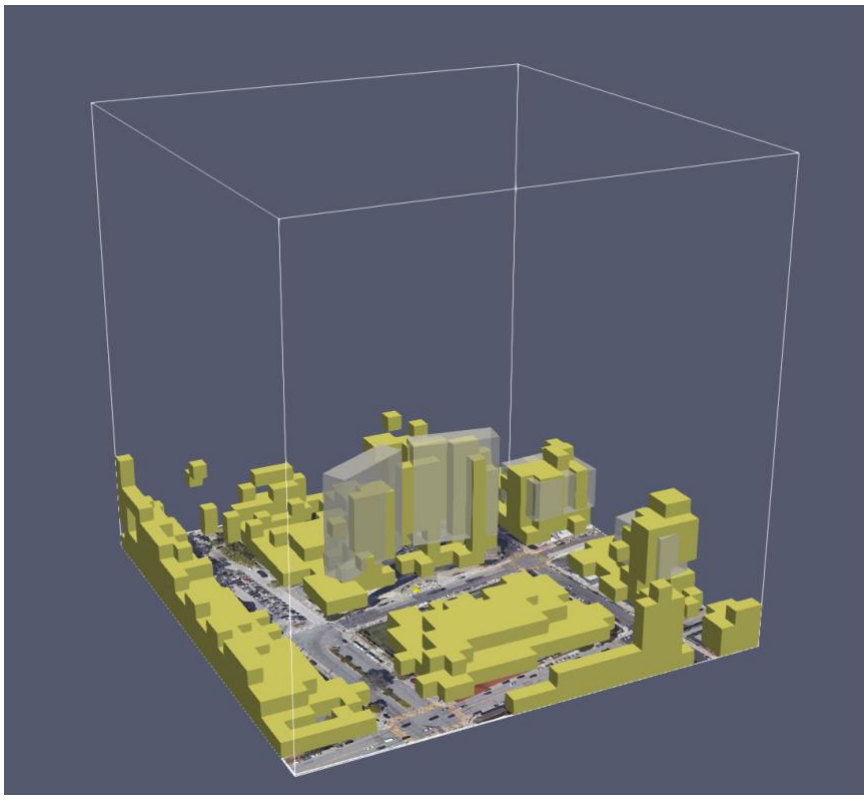

Fig. 32. Experimental result for combined voting algorithm.

6. Conclusions

GNSS multipath often remains the dominant source of error and uncertainty for many applications and especially for land vehicles operating in urban environments. This thesis examined two approaches for multipath detection and mitigation and also evaluated a method to generate 3D maps using LOS and NLOS GNSS rays.

6.1 Conclusions

Chapter 3 discussed a multipath detection and mitigation approach that uses 3D building maps and ray tracing to predict the presence of multipath signals at a given user location. This approach can identify multiple multipath signals simultaneously and does not require redundancy in GNSS measurements. Simulation and experimental results show that deterministic ray tracing is highly sensitive to error in initial user position estimate and building modeling errors. A stochastically determined model of the building dimensions which takes into account the uncertainty in user position and modeling error was found to improve the performance of ray tracing to detect multipath signals.
Chapter 4 detailed a second approach to multipath detection and mitigation which utilized multi-frequency signals to estimate multipath parameters from the auto-correlation function. The correlation of multipath parameters among different frequencies improved the estimation accuracy of multipath parameters compared to single-frequency multipath parameter estimation. Two mathematical formulations of the dual-frequency estimation problem were presented: 1) exponential and 2) in phase quadrature (IQ) formulation of the combined effects Simulation results show that mathematical representation of the estimation problem greatly affects the optimization algorithm's performance in

converging to the global optimal solution. The IQ formulation was shown to be less sensitive to convergence error compared to the exponential formulation.

In Chapter 5, the thesis examined a set of methods to generate 3D building maps using GNSS signals. Three probability-based voting algorithms were evaluated. All three algorithms rely on the GNSS signals' SNR measurements to classify the signals into LOS and NLOS. A statistical SNR model was used but classification errors are high. The combined voting algorithm demonstrates greater advantages than the other two algorithms in its ability to tolerate misclassification of LOS/NLOS and errors caused by insufficient data in the map generation process.

6.2 Future Work

Multipath detection using ray tracing and 3D building maps can be combined with the map generation algorithms to formulate a simultaneous localization and mapping (SLAM) problem to solve for user location and the 3D surroundings using GNSS signals.

The mathematical formulation of the dual-frequency multipath parameter estimation problem can be expanded to incorporate additional frequencies and signals. For GPS, the higher chipping rate of L5 signal results in better performance in multipath and may provide additional insight and benefit to the multipath estimation problem.

Multipath and NLOS signals can be better leveraged in the map generation algorithm by estimating reflection points on the reflector walls and using the reflection points to estimate obstable locations. A priori information of the surroundings can be incorporated into the map generation process to better aid the voting algorithms.

Bibliography

[1] Walter, T., Blanch, J., & Enge, P. (2012, September). L1/L5 SBAS MOPS to support multiple constellations. In *Proceedings of the 25th International Technical Meeting of the Satellite Division of the Institute of Navigation (ION GNSS)*.

[2] Thornberg, D. B., Thornberg, D. S., DiBenedetto, M. F., Braasch, M. S., Van Graas, F., & Bartone, C. (2003). LAAS integrated multipath-limiting antenna. *Navigation*, *50*(2), 117-130.

[3] Ray, J. K., Cannon, M. E., & Fenton, P. (2001). GPS code and carrier multipath mitigation using a multiantenna system. *IEEE Transactions on Aerospace and Electronic Systems*, *37*(1), 183-195.

[4] Meguro, J. I., Murata, T., Takiguchi, J. I., Amano, Y., & Hashizume, T. (2009). GPS multipath mitigation for urban area using omnidirectional infrared camera. *IEEE Transactions on Intelligent Transportation Systems*, *10*(1), 22-30.

[5] Seif, H. G., & Hu, X. (2016). Autonomous driving in the iCity—HD maps as a key challenge of the automotive industry. *Engineering*, *2*(2), 159-162.

[6] Pinana-Diaz, C., Toledo-Moreo, R., Bétaille, D., & Gómez-Skarmeta, A. F. (2011, October). GPS multipath detection and exclusion with elevation-enhanced maps. In *2011 14th International IEEE Conference on Intelligent Transportation Systems (ITSC)* (pp. 19-24). IEEE.

[7] Obst, M., Bauer, S., & Wanielik, G. (2012, April). Urban multipath detection and mitigation with dynamic 3D maps for reliable land vehicle localization.

In *Proceedings of the 2012 IEEE/ION Position, Location and Navigation Symposium* (pp. 685-691). IEEE.

[8] Miura, S., Hisaka, S., & Kamijo, S. (2013, October). GPS multipath detection and rectification using 3D maps. In *16th International IEEE Conference on Intelligent Transportation Systems (ITSC 2013)* (pp. 1528-1534). IEEE.

[9] Van Dierendonck, A. J., Fenton, P., & Ford, T. (1992). Theory and performance of narrow correlator spacing in a GPS receiver. *Navigation*, *39*(3), 265-283.

[10] Van Nee, R. D., Siereveld, J., Fenton, P. C., & Townsend, B. R. (1994, April). The multipath estimating delay lock loop: approaching theoretical accuracy limits. In *Proceedings of 1994 IEEE Position, Location and Navigation Symposium-PLANS'94* (pp. 246-251). IEEE.

[11] Townsend, B., & Fenton, P. (1994, September). A practical approach to the reduction of pseudorange multipath errors in a L1 GPS receiver. In *Proceedings of the 7th International Technical Meeting of the Satellite Division of the Institute of Navigation, Salt Lake City, UT, USA* (pp. 20-23).

[12] Mubarak, O. M., & Dempster, A. G. (2010). Analysis of early late phase in single- and dual-frequency GPS receivers for multipath detection. *GPS solutions*, *14*(4), 381-388.

[13] Groves, P. D. (2011). Shadow matching: A new GNSS positioning technique for urban canyons. *The journal of Navigation*, *64*(3), 417-430.

[14] Weissman, A., Ben-Moshe, B., Levi, H., & Yozevitch, R. (2013, March). 2.5 D mapping using GNSS signal analysis. In *2013 10th Workshop on Positioning, Navigation and Communication (WPNC)* (pp. 1-6). IEEE.

[15] Kim, K., Summet, J., Starner, T., Ashbrook, D., Kapade, M., & Essa, I. (2008, September). Localization and 3D reconstruction of urban scenes using GPS. In *2008 12th IEEE International Symposium on Wearable Computers* (pp. 11-14). IEEE.

[16] Irish, A. T., Isaacs, J. T., Quitin, F., Hespanha, J. P., & Madhow, U. (2014, May). Probabilistic 3D mapping based on GNSS SNR measurements. In *2014 IEEE International Conference on Acoustics, Speech and Signal Processing (ICASSP)* (pp. 2390-2394). IEEE.

[17] Lau, L., & Cross, P. (2007). Development and testing of a new ray-tracing approach to GNSS carrier-phase multipath modelling. *Journal of Geodesy*, *81*(11), 713-732.

[18] Brunner, F. K., Hartinger, H., & Troyer, L. (1999). GPS signal diffraction modelling: the stochastic SIGMA-Δ model. *Journal of Geodesy*, *73*(5), 259-267.

[19] Jan, S. S., Chan, W., Walter, T., & Enge, P. (2001, September). Matlab simulation toolset for SBAS availability analysis. In *Proceedings of the Institute of Navigation GPS* (Vol. 1).

[20] Misra, P., & Enge, P. (2006). Global Positioning System: signals, measurements and performance second edition. *Global Positioning System: Signals, Measurements And Performance Second Editions*, *206*.

[21] Blanch, J., Walter, T., Enge, P., Lee, Y., Pervan, B., Rippl, M., & Spletter, A. (2012, September). Advanced RAIM user algorithm description: integrity support message processing, fault detection, exclusion, and protection level calculation. In *Proceedings of the 25th International Technical Meeting of The Satellite Division of the Institute of Navigation (ION GNSS 2012)* (pp. 2828-2849).

[22] Abdi, A., Lau, W. C., Alouini, M. S., & Kaveh, M. (2003). A new simple model for land mobile satellite channels: first-and second-order statistics. *IEEE Transactions on Wireless Communications*, *2*(3), 519-528.

[23] Loo, C. (1985). A statistical model for a land mobile satellite link. *IEEE transactions on vehicular technology*, *34*(3), 122-127.